

# We are IntechOpen, the world's leading publisher of Open Access books Built by scientists, for scientists

6,900

Open access books available

186,000

International authors and editors

200M

Downloads

Our authors are among the

154

Countries delivered to

TOP 1%

most cited scientists

12.2%

Contributors from top 500 universities



WEB OF SCIENCE™

Selection of our books indexed in the Book Citation Index  
in Web of Science™ Core Collection (BKCI)

Interested in publishing with us?  
Contact [book.department@intechopen.com](mailto:book.department@intechopen.com)

Numbers displayed above are based on latest data collected.  
For more information visit [www.intechopen.com](http://www.intechopen.com)



---

# Electronic Structure and Topological Quantum Phase Transitions in Strained Graphene Nanoribbons

---

Fanyao Qu, Ginetom S. Diniz and Marcos R. Guassi

Additional information is available at the end of the chapter

<http://dx.doi.org/10.5772/64493>

---

## Abstract

In this chapter, we discuss the new classes of matter, such as the quantum spin Hall (QSH) and quantum anomalous Hall (QAH) states, that have been theoretically predicted and experimentally observed in graphene and beyond graphene systems. We further demonstrate how to manipulate these states using mechanical strain, internal exchange field, and spin-orbit couplings (SOC). Spin-charge transport in strained graphene nanoribbons is also discussed assuming the system in the QAH phase, exploring the prospects of topological devices with dissipationless edge currents. A remarkable zero-field topological quantum phase transition between the time-reversal-symmetry-broken QSH and quantum anomalous Hall states is predicted, which was previously thought to take place only in the presence of external magnetic field. In our proposal, we show as the intrinsic SOC is tuned, how it is possible to two different helicity edge states located in the opposite edges of the graphene nanoribbons exchange their locations. Our results indicate that the strain-induced pseudomagnetic field could be coupled to the spin degrees of freedom through the SOC responsible for the stability of a QSH state. The controllability of this zero-field phase transition with strength and direction of the strain is also explored as additional phase-tuning parameter. Our results present prospect of strain, electric and magnetic manipulation of the QSH, and QAH effect in these novel two-dimensional (2D) materials.

**Keywords:** Graphene, graphene nanoribbon, quantum spin Hall, quantum anomalous Hall, topological insulator, 2D materials, strain

---

## 1. Introduction

Starting from the work by Landau and Peierl's work [1, 2], two-dimensional (2D) materials were regarded as theoretical structures, thermodynamically unstable to be obtained in

---

laboratory. This is because of fusion temperature decreases as function of thickness of thin films, causing the material to segregate in islands or decomposing in typically thicknesses of tens of atomic layers [3, 4]. In 1947, Wallace [5] demonstrated the electronic properties of what became the first theoretical work predicting the one-atom thick of carbon atoms. Past 57 years, his theoretical predictions were experimentally synthesized by Novoselov et al., which now is widely known as graphene. In 2004, Geim and Novoselov [6, 7] created by mechanical exfoliation an one-atom thick layer made of graphite, the so-called graphene. Due to their well-succeeded experiment, many other techniques have been developed to grow graphene on several possible substrate materials such as on hydrogenated silicon carbide, copper, cobalt, and gold [8–16].

Before 2004, graphite systems were also widely studied [5, 17, 18], and their electronic properties used to theoretically describe other materials based on carbon, such as fullerene [19] and carbon nanotubes [20]. These chemical elements have attracted much attention because of their exotic electronic and mechanical properties, such as high tensile strength and, in the case of nanotubes, tunable electronic structure according to chirality, radius, and high thermal conductivity. A new type of derivative of graphene arose after 2004: the graphene nanoribbon [21], in which some electronic properties of the graphene were modified and could be controlled. These properties depends on the type of crop that was carried out on graphene and can be simpler cuts, called zigzag and armchair or being modeled in a specific way, such as triangles to form quantum dots [21–25] or even with Z formats [26].

The interest in two-dimensional materials started from the nineteenth century, mainly for its electronic transport properties after the discovery of the Hall effect. In 1988, Haldane predicted that another type of Hall effect, called anomalous quantum Hall effect, could be observed in a two-dimensional crystal with hexagonal lattice [27]. Recently, the new classes of matter, such as quantum Hall effect (QHE) [28, 29], quantum anomalous Hall (QAH) effect [30–32], and quantum spin Hall (QSH) effect [33, 34], have been discovered or predicted in the graphene, as well as other 2D materials such as topological insulators [35–37], HgTe-CdTe quantum wells [38, 39], silicene [40], two-dimensional germanium [40], and transition metal dichalcogenides [41]. Among these new classes of matter, the QSH and QAH states possess topologically protected edge states at the boundary, where the electron backscattering is forbidden, offering a potential application to electronic devices to transport current without dissipation [24, 42]. However, the QSH state and QAH are very different states of matter. The quantum spin Hall is characterized by a gap completely insulating the bulk, and their edge states are helical with no gap, wherein opposite spins propagate in opposite directions on each side of the sample and are protected by time reversal symmetry (TRS) [27, 33, 36, 38–40, 43, 44]. In the case of quantum anomalous Hall, chiral edge states takes place, also without gap, where one spin channel is suppressed because of the TRS break [35, 37, 45]. Therefore, to observe topological phase transitions (QPT) between quantum spin Hall and quantum anomalous Hall states, it is necessary to apply a condition, which might break the TRS [28]. An external magnetic field is a potential solution but from applicability point of view, an internal exchange field (EX) which takes the main spin band to be completely filled while the minority spin band becomes empty, becomes an more attractive alternative [31, 32, 35, 46]. As

it is known, a pseudo-magnetic field induced by strain  $B_s$  leads to Landau quantization and edge states that circulate in opposite directions [47, 48], and the strain creates graphene pseudo-magnetic fields. Then, without breaking the TRS, the strain may induce a gap in the bulk and edges without helical gap. Thus, strain, EX and SOC can be used as a versatile tool for control of topological phase transitions [32]. These facts motivated us to propose ways in which the spin-orbit coupling, uniaxial mechanical strain and exchange (instead of an external magnetic field) to be used to carry out phase transitions in graphene nanoribbons [49].

In this chapter, firstly, we make a brief description on tight-binding model. Then, we report energy band structure of the graphene and the individual effects of the intrinsic SOC, the Rashba SOC, and the EX. After that, we present the effects of applied uniaxial strain on both electronic structure and transport property of the graphene. Then, we demonstrate the effects of strain on single-particle energy and quantum transport property of graphene nanoribbons. Finally, we show systematically the strain-engineered QPT from the QSH to QAH states.

## 2. Electronic structure and transport properties of graphene

### 2.1. Electronic structure of graphene tight-binding approach

An isolated atom has its own electronic levels ranging and depending on its fundamental characteristics. When two or more atoms are approximate to each other, their electronic levels are recombined to obtain a new structure for the system as a whole. And the periodic clustering of atoms in a structure is meant by the crystal lattice. In the case of an insulating material, superposition of the wave functions of the valence electrons in the crystal lattice atoms is low. In the case of a conductive material, such superposition of the wave function of the electrons is large and acquires great mobility through the solid. Semiconductor materials have an electronic distribution that is not very well located, because there is not a too strong electrical attraction between electrons and protons on the atomic nucleus but low overlap between the valence electrons from neighboring atoms are observed. The tight-binding method is useful in those cases [50]. Thus, one can assume that the lattice Hamiltonian  $\hat{H}_{\text{latt}}$  can be approximated in the vicinity of each point of the grid system by Hamiltonian  $\hat{H}$  of the atom located at that point. However, this has some disadvantages, because this method does not allow us to include continuous spectra and also does not have good description for levels below the valence states.

In order to apply tight-binding method to graphene, we begin with the wave function of an electron on its lattice as a linear combination of atomic orbitals of A and B sites, the two distinct atoms in graphene unit cell

$$|\Psi\rangle = \alpha(\vec{k})|\phi_A, s\rangle + \beta(\vec{k})|\phi_B, s'\rangle; \quad (1)$$

where  $\alpha(\vec{k})$  and  $\beta(\vec{k})$  are coefficients,  $s$  is the spin projection, and Bloch functions are

$$|\phi_c\rangle = \frac{1}{\sqrt{N}} \sum_n e^{i\vec{k}\cdot\vec{R}_n} |C_n, s\rangle \tag{2}$$

where  $C=A,B$ . In these functions,  $\vec{R}_n$  is an carbon atom position concerning the origin of coordinate system, the exponential carries the periodicity of the lattice;  $\frac{1}{\sqrt{N}}$  is the normalization factor ( $N$  is the number of atoms in graphene).

Lattice Hamiltonian are made up of two terms: on-site  $\hat{H}_{on}$  and hopping  $\hat{H}_h$  energy

$$\hat{H}_{latt} = \hat{H}_{on} + \hat{H}_h \tag{3}$$

The first one,  $\hat{H}_{on}$  is

$$\hat{H}_{on} = \epsilon_0 \sum_n \{ |A_n\rangle \langle A_n| + |B_n\rangle \langle B_n| \}; \tag{4}$$

with  $A$  and  $B$  representing sites, nonequivalent types of carbon atoms on the unit cell. This energy can be set as  $\epsilon_0=0$  at Fermi level and the term vanishes. Here, the spin index was suppressed because only identical spins couple. The term  $\hat{H}_h$  defines the hopping of electrons between nearest-neighbor atoms, since we use first-neighbors tight-binding approach.

$$\hat{H}_h = -\sum_{\langle i,j \rangle} t_{ij} ( |A_i\rangle \langle B_j| + |B_j\rangle \langle A_i| ); \tag{5}$$

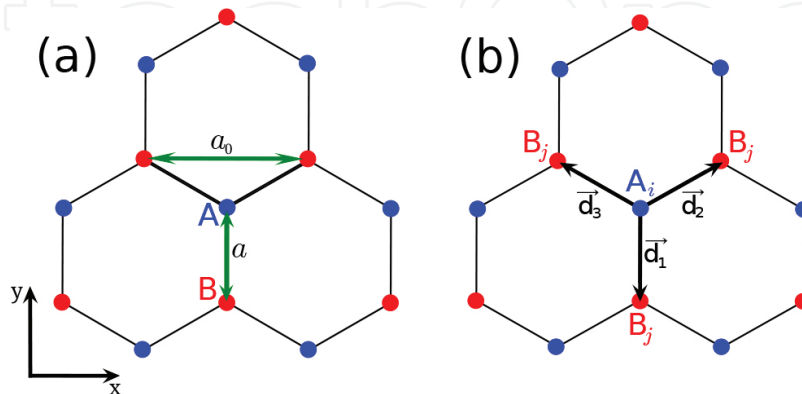


**Figure 1.** (a) Distance between two carbon atoms  $a$  and lattice constant  $a_0$ . (b) Nearest-neighbors of an A site. Copyright (2015) by the American Physical Society [49].

where  $i$  and  $j$  are site index and summation over  $\langle i, j \rangle$  indicates only nearest neighbor atoms are being considered. The  $t_{ij}$  is called hopping factor and gives probability amplitude of an electron on  $i$  site hop to a  $j$  site. Its value is the same for each nearest neighbor  $t_{ij}=2.7eV$  [51, 52]. The distance vectors from an A site to their nearest neighbors are, as one can see in **Figure 1**,

$$\vec{d}_1 = -a\hat{y}, \quad \vec{d}_2 = +\frac{a_0}{2}\hat{x} + \frac{a}{2}\hat{y} \quad \text{and} \quad \vec{d}_3 = -\frac{a_0}{2}\hat{x} + \frac{a}{2}\hat{y} \quad (6)$$

and B-site distance vector can be obtained in a similar way. Here,  $\hat{x}$  and  $\hat{y}$  are the unitary vectors along x axis and y axis. The distance between two carbon atoms is  $a=0.142$  nm, and  $a_0=\sqrt{3}a$  is the lattice constant.

To find energy equations for our system, we solve Schrödinger's equation using Eqs. (1) and (5). This will give

$$E\alpha(\vec{k}) = -t \left[ e^{ik_y a} + 2\cos\left(\frac{k_x a_0}{2}\right) e^{-ik_y a/2} \right] \beta(\vec{k}), \quad (7)$$

$$E\beta(\vec{k}) = -t \left[ e^{-ik_y a} + 2\cos\left(\frac{k_x a_0}{2}\right) e^{ik_y a/2} \right] \alpha(\vec{k}); \quad (8)$$

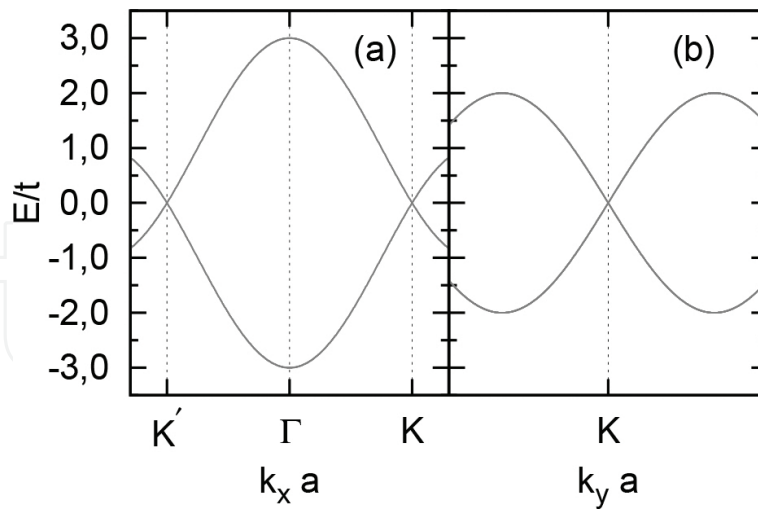


**Figure 2.** Energy band of graphene (a) along  $k_y=0$  and (b)  $k_x=4\pi / 3\sqrt{3}$  directions.

In **Figure 2**, valence and conduction bands are shown in profile: with  $k_y=0$  in (a), where symmetric points  $K, K'$ , and  $\Gamma$  are shown; and  $k_x=4\pi / 3\sqrt{3}$  in (b), showing  $K$  point. In both cases, no bandgap is observed in the graphene.

Quantum anomalous Hall and quantum spin Hall effect can be induced in graphene without a magnetic field if we consider Rashba and intrinsic spin-orbit coupling and also exchange field [53, 54]. Intrinsic spin-orbit coupling is weak on graphene [55–57], however, graphene is easily affected by disturbance at low energies and the effects due to spin-orbit coupling should become relevant at low temperatures [33]. Although it is challenging the experimental envision, this type of coupling can be controlled with graphene deposition on other materials. The exchange interaction that occurs between electron spins can be observed in graphene with stabilization of a ferromagnetic phase, when it has a low doping [53, 58].

The intrinsic spin-orbit interaction evolves the next nearest-neighbors and is written as

$$\hat{H}_{so} = \frac{2i}{\sqrt{3}} \lambda_{so} \sum_{\langle\langle i,j \rangle\rangle} \sum_{ss'} \{ |A_i, s\rangle \vec{\gamma} \cdot (\vec{d}_{kj} \times \vec{d}_{ik}) \langle A_j, s' | + h.c. \} \quad (9)$$

being  $\lambda_{so}$  the strength parameter, estimated up to 2.4 K [33]. Here, the  $s$  and  $s'$  are the  $z$ -components of real spin, and the summation  $\langle\langle i,j \rangle\rangle$  is over the next nearest-neighbors of a carbon atom, as shown in **Figure 3(a)**, the vectors  $d_{mn}$  indicate the distances between an atom on  $m$  site and another on  $n$  site, as shown in **Figure 3(b)**. To find energy equations for the SOC, we solve Schrödinger's equation using Eqs. (1) and (9). It leads to

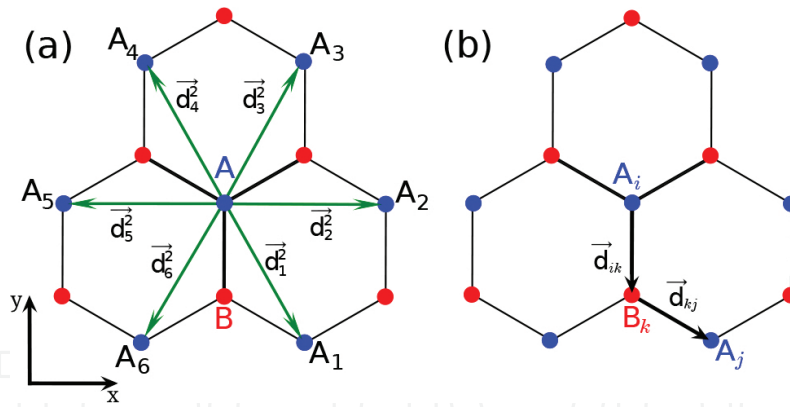


**Figure 3.** Next nearest-neighbors distance vectors of an A site (a). Definition of  $\vec{d}_{kj}$  and  $\vec{d}_{ik}$  vectors used in Hamiltonian 9. Figure adapted from Guassi et al. [49].

$$E\alpha(\vec{k}) = -4\lambda_{so}\alpha(\vec{k})\sin\left(\frac{k_x a_0}{2}\right) \left[ \cos\left(k_y \frac{3}{2}a\right) - \cos\left(\frac{k_x a_0}{2}\right) \right] s_z \quad (10)$$

and the negative of right side for  $\beta(\vec{k})$ . Clearly, **Figure 4** shows that an increase in parameter strength  $\lambda_{so}$  increases the gap of graphene, which is associated with a massive term in the Dirac-like Hamiltonian [59].

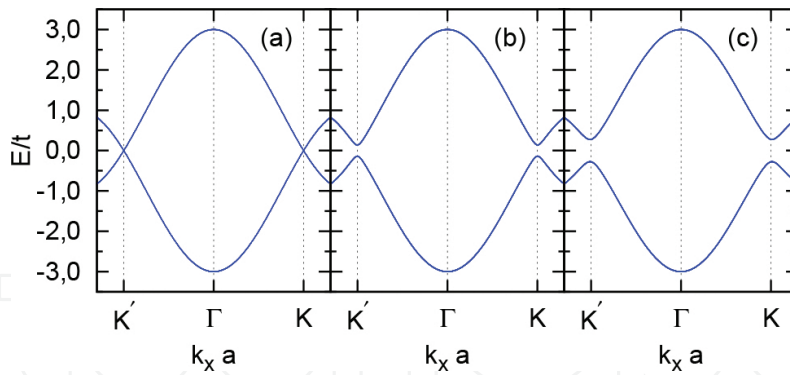


**Figure 4.** Energy band along  $k_y=0$  direction of graphene with (a)  $\lambda_{so}=0$ , (b)  $\lambda_{so}=0.03t$ , and (c)  $\lambda_{so}=0.06t$ .

Rashba spin-orbit coupling can be induced in graphene with application of an external electric field perpendicular to the sheet plane [60], interaction of carbon atoms with a substrate [43] or by curving the sheet [61–63]. Its Hamiltonian reads

$$\hat{H}_R = i \sum_{\langle ij \rangle} \sum_{ss'} \{ |A_i, s\rangle \langle \vec{u}_{ij} \cdot \vec{\gamma} | \langle B_j, s' | + h.c. \} \quad (11)$$

where the summation  $\langle i, j \rangle$  is over the nearest-neighbors of a carbon atom,  $\vec{\gamma}$  is the vector whose components are the Pauli spin matrices,  $\vec{u}_{ij}$  are defined by [60]

$$\vec{u}_{ij} = \frac{e}{2m^2av_F} \vec{E} \times \vec{R}_{ij} = -\frac{\lambda_R}{a} \hat{k} \times \vec{R}_{ij}, \quad (12)$$

with  $e$  the electron charge,  $m$  the rest mass of the electron, and  $v_F$  the Fermi velocity. The vector  $\vec{R}_{ij} = \vec{R}_j - \vec{R}_i$  gives difference between two atom positions on the lattice. Observing **Figure 1**, the vector  $\vec{R}_{ij}$  can be renamed to  $\vec{d}_l$ , with  $(l=1, 2, 3)$ .

Using electron wave function, Eq. (1) and Hamiltonian part 11, we find four spin nondegenerated energy equations:

$$E\alpha(\vec{k}, \uparrow) = i\lambda_R \left[ e^{ik_y a} + 2\cos\left(\frac{k_x a_0}{2} + \frac{2\pi}{3}\right) e^{-ik_y a/2} \right] \beta(\vec{k}, \downarrow) \quad (13)$$

$$E\beta(\vec{k}, \uparrow) = i\lambda_R \left[ e^{-ik_y a} + 2\cos\left(\frac{k_x a_0}{2} - \frac{2\pi}{3}\right) e^{ik_y a/2} \right] \alpha(\vec{k}, \downarrow) \quad (14)$$

$$E\alpha(\bar{k}, \downarrow) = i\lambda_R \left[ e^{ik_y a} + 2\cos\left(\frac{k_x a_0}{2} - \frac{2\pi}{3}\right) e^{-ik_y a/2} \right] \beta(\bar{k}, \uparrow) \tag{15}$$

$$E\beta(\bar{k}, \downarrow) = -i\lambda_R \left[ e^{-ik_y a} + 2\cos\left(\frac{k_x a_0}{2} + \frac{2\pi}{3}\right) e^{ik_y a/2} \right] \alpha(\bar{k}, \uparrow) \tag{16}$$

which, together with energy Eqs. (7) and (8), allow one to plot energy levels in **Figure 5**. As one can note, the Rashba SOC lifts the spin degeneracy, breaking the SU(2) symmetry. However, due to time-reversal symmetry, we still have  $E(k, \uparrow) = E(-k, \downarrow)$ .

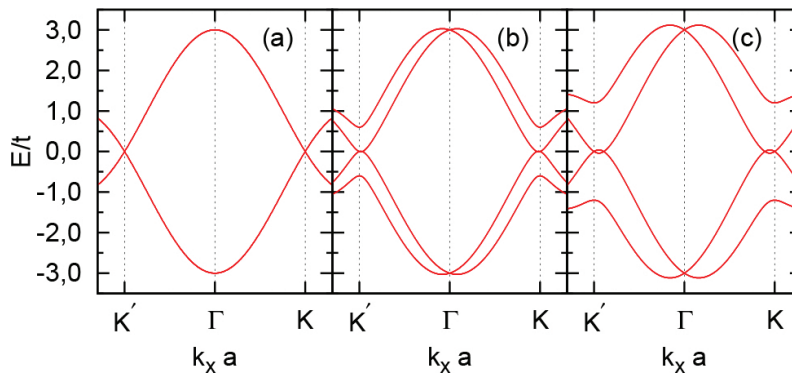


**Figure 5.** Energy band along  $k_y=0$  direction of graphene with (a)  $\lambda_R=0$ , (b)  $\lambda_R=0.20t$ , and (c)  $\lambda_R=0.40t$ .

Calculations of *ab initio* have recently shown that graphene doped with Fe on its surface may have intrinsic ferromagnetism [30]. This interaction arises when the change in the spin of an electron changes the electrostatic repulsion between electrons near it. Its Hamiltonian includes the coupling of orbital motion and the spin of the electrons with the exchange field. In this paper, to simplify the calculations and not lose generality, only the portion of spin will be considered. Now, the Hamiltonian is

$$H_{ex} = M \sum_{i;s} \{ |C_i, s\rangle \gamma_z \langle C_i, s| + h.c. \}, \tag{17}$$

where  $C=A,B$ ; strength parameter  $M$  is proportional to  $J_{eff} \mu'_z$ , where  $J_{eff}$  is the exchange interaction and  $\mu'_z$  is effective magnetic momentum of electron that associates to the exchange field. Thus,  $H_{ex}$  describes the magnetic momentum response of spin of an electron to the exchange field, like in Zeeman effect [45]. The  $\gamma_z$  is the Pauli matrix. This part of Hamiltonian gives energies

$$E\alpha(\vec{k}, \uparrow) = M\alpha(\vec{k}, \uparrow), \quad (18)$$

$$E\alpha(\vec{k}, \downarrow) = -M\alpha(\vec{k}, \downarrow); \quad (19)$$

the same for  $\beta(\vec{k}, s)$ . Combining with Eqs. (7) and (8), we can obtain the energy dispersion. In **Figure 6**, it clearly shows that the time-reversal symmetry is broken, since  $E(\vec{k}, \uparrow) \neq E(-\vec{k}, \downarrow)$ . Initially, one might think that graphene nanoribbon subject to an exchange field should not bear the quantum spin Hall state, as this would be protected by the time-reversal symmetry [33, 43]. But it has been found a similar state, called pseudo-Hall quantum spin state or quantum spin Hall state with broken time-reversal symmetry [45] in which was possible to observe the spin polarized current on the edges of nanoribbon. In addition, the exchange field is critical to control the transition between electronic states of quantum anomalous Hall to quantum spin Hall [49].

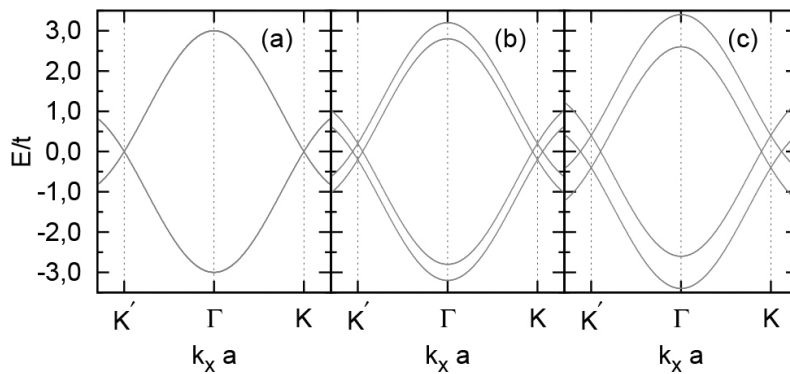


**Figure 6.** Energy band along  $k_y = 0$  direction of graphene with (a)  $M = 0$ , (b)  $M = 0.20t$ , and (c)  $M = 0.40t$ .

## 2.2. Electronic structure of strained graphene

Deformation can naturally be observed when graphene is grown on top of other materials, because of distinct atomic arrangements between the atoms of graphene and the substrate. The application of an external tension on graphene sheet or nanoribbons can change its electronic properties, as with the nanotubes [64–68]. Some calculations [69] and experiments [70] have shown that these deformations can reach about 20% of the initial interatomic distance without permanently deform the graphene.

Strain is calculated in graphene using the strain matrix defined in [52]:

$$\epsilon = \varepsilon \begin{pmatrix} \cos^2\theta - \nu\sin^2\theta & (1+\nu)\cos\theta\sin\theta \\ (1+\nu)\cos\theta\sin\theta & \sin^2\theta - \nu\cos^2\theta \end{pmatrix} \quad (20)$$

where  $\epsilon$  is strain modulus,  $\theta$  is the direction of strain,  $\theta=0$  being parallel to a zigzag chain and  $\nu=0.165$  is the Poisson ratio [71]. Therefore, matrix elements read,

$$\epsilon_{11} = \epsilon[\cos^2\theta - \nu\sin^2\theta] \quad (21)$$

$$\epsilon_{12} = \epsilon[(1 + \nu)\cos\theta\sin\theta] \quad (22)$$

$$\epsilon_{21} = \epsilon[(1 + \nu)\cos\theta\sin\theta] \quad (23)$$

$$\epsilon_{22} = \epsilon[\sin^2\theta - \nu\cos^2\theta] \quad (24)$$

The transformation of an atom position from  $(x, y)$  to the new position  $(x', y')$  after the strain application will be

$$\begin{pmatrix} x' \\ y' \end{pmatrix} = \begin{pmatrix} (1 + \epsilon_{11}) & \epsilon_{12} \\ \epsilon_{21} & (1 + \epsilon_{22}) \end{pmatrix} \begin{pmatrix} x \\ y \end{pmatrix}. \quad (25)$$

Or, in vectorial form

$$\vec{d}^s = (I + \epsilon)\vec{d} \quad (26)$$

where  $\vec{d}$  and  $\vec{d}^s$  are the vectors that defines the nearest-neighbor in the graphene without and with application of the strain,  $I$  is identity matrix, and  $\epsilon$  is the matrix 20.

Hopping term  $t$  is also modified by strain [52]

$$t_{i,j} = t_i = te^{-3.37(\vec{d}_i^s/a-1)}. \quad (27)$$

With these modifications, energy equations for strained graphene are calculated in the same way as in Section 2.1 and gives

$$E\alpha(\vec{k}) = -\sum_l^3 t_l \exp\{i\vec{k} \cdot \vec{d}_l^s\} \alpha(\vec{k}) \quad (28)$$

with summation made over the nearest-neighbors. For  $\beta(\vec{k})$ , the expression is the complex hermitian of  $\alpha(k)$ . **Figure 7** shows the contour plot of valence band subjected to a strain with

modulus of 15% along zigzag chains, i.e.,  $\theta=0$  (a) and toward the armchair chains, i.e.,  $\theta=\pi/2$  (b). Notice that no bandgap is opened up in both cases [52]. Nevertheless, the form of the 1st BZ has been deformed by the strain. Therefore, the Dirac points  $K$  and  $K'$  are the strain shifted. The new positions of the deformed Dirac cones are well determined by the following equation [72]:

$$\vec{K} \cdot (\vec{d}_1^s - \vec{d}_2^s) = \arccos\left(\frac{t_3^2 - t_1^2 - t_2^2}{2t_1t_2}\right) \quad (29)$$

where  $\vec{K} = (K_x, K_y)$

$$H_{so} = \frac{2i}{\sqrt{3}} \lambda_{so} \sum_{\langle\langle i,j \rangle\rangle} \sum_{ss'} \{ |A_i, s\rangle \vec{\gamma} \cdot (\vec{d}_{kj}^s \times \vec{d}_{ik}^s) \langle A_j, s' | + h.c. \} \quad (30)$$

now, with new distances  $\vec{d}_{ik}^s$ , modified by strain. This will give us new energies expressions,

$$E\alpha(\vec{k}, \uparrow) = i\lambda_{so}\mu \sum_l^3 \sigma_l \left( e^{i\vec{k} \cdot \vec{d}_l^{s2}} - e^{-i\vec{k} \cdot \vec{d}_l^{s2}} \right) \alpha(\vec{k}, \uparrow) \quad (31)$$

and nearly the same for other expressions, with

$$\alpha(\vec{k}, \uparrow) = -\alpha(\vec{k}, \downarrow) = -\beta(\vec{k}, \uparrow) = \beta(\vec{k}, \downarrow) \quad (32)$$

In Eq. (31),  $\vec{d}_l^{s2}$  are the vectors between the next nearest-neighbor sites and

$$\mu = (1 + \epsilon_{11})(1 + \epsilon_{22}) + \epsilon_{12}\epsilon_{21} \quad (33)$$

In **Figure 8**, we show the effects of the combination of intrinsic SOC and uniaxial strain applied along  $\theta=0$  direction for different strain modulus  $\epsilon$  and  $\lambda_R=0.0$ . The bandgap generated by the intrinsic SOC is still present, although as strain is increased the bandgap reduces, the energy dispersion can also displays different features as the direction of applied strain is varied [52]. The Rashba Hamiltonian can include strain as well, and this will leave us with equations

$$E\alpha(\vec{k}, \uparrow) = -i\varphi_{s-} \beta(\vec{k}, \downarrow) \quad (34)$$

$$E\alpha(\vec{k}, \downarrow) = -i\varphi_{s+}^* \beta(\vec{k}, \uparrow) \quad (35)$$

$$E\beta(\vec{k}, \uparrow) = i\varphi_{s+}\alpha(\vec{k}, \downarrow) \tag{36}$$

$$E\beta(\vec{k}, \downarrow) = i\varphi_{s-}^*\alpha(\vec{k}, \uparrow) \tag{37}$$

where

$$\varphi_{s-} = \lambda_R \left\{ \rho_1 e^{-3i\xi_1} - \rho_1 \cos(\xi_2) + \sqrt{3}\rho_2 \sin(\xi_2) \right\} e^{i\xi_1} \tag{38}$$

$$\varphi_{s+} = \lambda_R \left\{ \rho_1 e^{3i\xi_1} - \rho_1 \cos(\xi_2) - \sqrt{3}\rho_2 \sin(\xi_2) \right\} e^{-i\xi_1} \tag{39}$$

and we defined

$$\rho_1 = 1 + \epsilon_{22} + i\epsilon_{12} \tag{40}$$

$$\rho_2 = 1 + \epsilon_{11} - i\epsilon_{21} \tag{41}$$

$$\xi_1 = \frac{k_x a}{2} \epsilon_{12} + \frac{k_y a}{2} (1 + \epsilon_{22}) \tag{42}$$

$$\xi_2 = \frac{k_x a_0}{2} (1 + \epsilon_{11}) + \frac{k_y a_0}{2} \epsilon_{21} \tag{43}$$

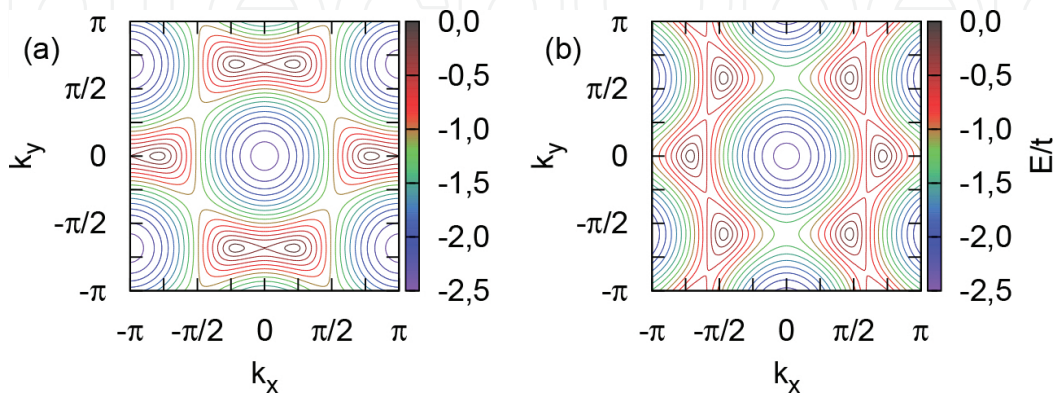
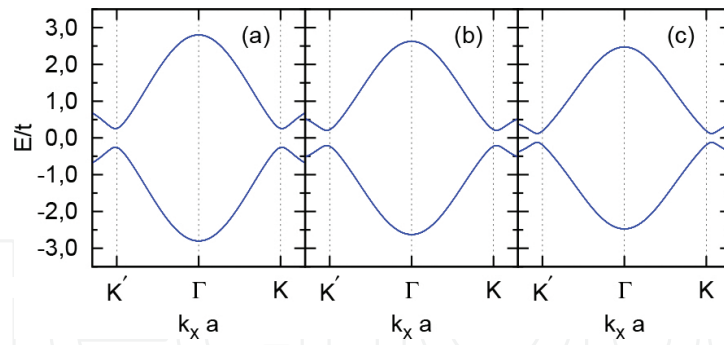
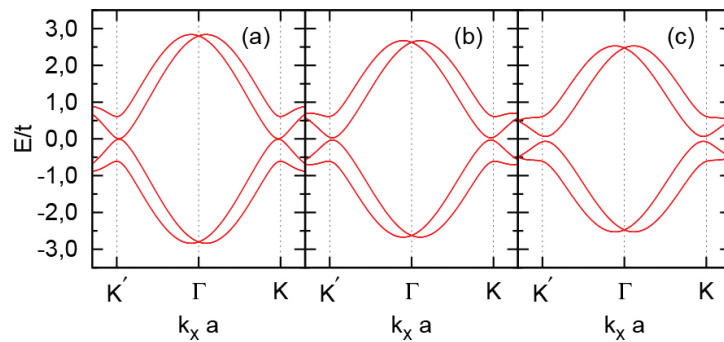


Figure 7. Contour plot of valence band of strained graphene with  $\epsilon = 0.15$  for  $\theta = 0$  (a) and  $\pi / 2$  (b).



**Figure 8.** Energy band of strained graphene with  $\lambda_s o = 0.06t$  and  $\theta = 0$ , for  $\epsilon = 0.05$  (a),  $\epsilon = 0.10$  (b),  $\epsilon = 0.15$  (c). Here, we have set  $\lambda_R = 0.0$ .



**Figure 9.** Energy band of strained graphene with  $\lambda_R = 0.20t$  and  $\theta = 0$ , for  $\epsilon = 0.05$  (a),  $\epsilon = 0.10$  (b),  $\epsilon = 0.15$  (c).

In **Figure 9**, we can still observe the broken spin-degeneracy, but compared with the case where the uniaxial strain is absent, one can note that the effect of strain is to renormalize the Rashba SOC and shifts the Dirac point relative to the original one.

### 2.3. Quantum anomalous Hall effect in strained graphene

In this section, we discuss the prospects of external manipulation of the quantum anomalous Hall effect (QAHE) in graphene by strains [73–76]. We present here our results of the microscopic study of the QAHE in graphene under uniaxial strains [32]. For this purpose, we have theoretically explored the dependence of electronic structure, topological and transport properties upon the orientation and modulus of uniaxial strain, in the presence of Rashba, Intrinsic SO, and an exchange field interaction [32].

To identify the topological properties of the Dirac gap and study the origin of QAHE, we have calculated the Berry curvature of the  $n$ th bands  $\Omega_{xy}^n(k_x, k_y)$  using the Kubo formula:

$$\Omega_{xy}^n(k_x, k_y) = -\sum_{n' \neq n} \frac{2\text{Im}\langle \Psi_{nk} | v_x | \Psi_{n'k} \rangle \langle \Psi_{n'k} | v_y | \Psi_{nk} \rangle}{(\omega_{n'} - \omega_n)^2} \quad (44)$$

where  $\omega_n = E_n / \hbar$  with  $E_n$  the energy eigenvalue of the  $n$ th band and  $v_{x(y)} = \hbar^{-1} \partial H / \partial k_{x(y)}$  is the Fermi velocity operator. When the Fermi level lies within the bulk gap, i.e., in the insulating regime, according to the Kubo formula, the corresponding Hall conductance is quantized as  $\sigma_{xy} = C e^2 / h$ , where  $C$  is defined as the Chern number and can be calculated by [77]

$$C = \frac{1}{2\pi} \sum_n \int_{BZ} d^2 k \Omega_{xy}^n, \quad (45)$$

where the summation is taken over all the occupied states below the Fermi level, and the integration is carried out over the whole first Brillouin zone.

Since the Berry curvatures are highly peaked around the Dirac points  $\mathbf{K}$  and  $\mathbf{K}'$  [78], then a low energy approximation can be used in the calculation of the Chern number [30]. This allows us to derive an effective tight-binding Hamiltonian of the strained graphene, by expanding  $H(\mathbf{k})$  at the vicinity of the strain-shifted Dirac points, i.e.,  $\mathbf{k} = \eta \mathbf{K} + \mathbf{q}$ , where  $\eta = \pm 1$  labels the two valleys, and  $\mathbf{q} = (q_x, q_y)$  is a small crystal momentum around  $\eta \mathbf{K}$ . The validity of the low energy approximation requires the strain modulus to be upper limited, such that does not go beyond the threshold of an appearance of a band gap, thus the band is still linear and gapless at the strain-shifted Dirac points, in the absence of SOCs and exchange field interactions [79]. This condition is fulfilled by the relation on the strain-dependent hopping parameters  $|t_1 - t_2| \leq t_3 \leq |t_1 + t_2|$ , where  $t_{i=1,2,3}$  is the hopping along each C-C bond [80]. Under this condition, we calculate the Chern number using the following equation:

$$C = \frac{1}{2\pi} \sum_{\mathbf{K}, \mathbf{K}'} \sum_{n=1,2} \int_{-\infty}^{\infty} dq_x dq_y \Omega_{xy}^n(q_x, q_y) \quad (46)$$

It is interesting to mention that in the above integral, a momentum cutoff is set around each valley for which the Chern number calculation is guaranteed to converge.

As known, intrinsic spin-orbit (ISO) interaction respects the crystal symmetries and does not couple states of opposite spins. But it opens up a topologically nontrivial bulk band gap at zero magnetic field [43]. This bulk band gap hosts two counter-propagating edge modes per edge in the graphene nanoribbon, with opposite spins: this topological phase is known as the QSH phase and may be regarded as two opposite QH phases (i.e., each spin performs the QH effect, with opposite chirality) [27]. Therefore, the Chern number must vanish in a system with TRS. In contrast, the Rashba term explicitly violates the  $z \rightarrow -z$  mirror symmetry. Moreover, it mixes different spin components and depresses the ISO induced band gap [81]. When the exchange field is applied and only ISO is turned on, the combination of the ISO coupling and exchange field leads to the breaking of the TRS which is preserved in the QSH phase. However, due to the absence of spin-flip terms in the Hamiltonian, the helical edge-state structure persists. Thus, both the Chern number and the conductance are equal to zero. Unlikely, when

Rashba SOC is considered, in addition to ISO and exchange field, the system can be in a regime, which depends on  $\lambda_R$ ,  $\lambda_{so}$ , and  $M$  parameters, that may result in a phase transition from zero conductance to finite conductance [32].

Let us now calculate the Hall conductivity of the strained graphene considering both Rashba SOC and ISO. **Figure 10(a)** and **(b)** shows the Hall conductance for  $\lambda_R(\varepsilon=0)=0.1t$  and  $\lambda_{so}(\varepsilon=0)=0.06t$  along  $\theta=0$  and  $\theta=\pi/2$ , respectively. One can clearly note the two distinct phases: Insulating (I) characterized by  $C=0$  and the QAHE phase with  $C=2$ , where  $C=C_k+C_{k'}$ . The two different phases can be accessed by appropriately tuning the exchange field  $M$  and the strain modulus  $\varepsilon$ . **Figure 10(d)** shows the dependence of the Hall conductance  $\sigma_{xy} = Ce^2/h$  on the exchange field and the strain parameters with  $\theta=\pi/2$  for  $\lambda_R(\varepsilon=0)=0.1t$  and  $\lambda_{so}(\varepsilon=0)=0.06t$ . We find that a finite ISO drives a phase transition from QAHE to an insulator phase [32]. We also notice that for  $M$  being smaller than  $0.24t$ , the conductance  $\sigma_{xy}$  of unstrained graphene is equal to zero, corresponding to an insulator phase in the graphene, also called a time-reversal-symmetry-broken quantum spin-Hall phase [34]. At  $M_c=0.24t$ , an abrupt change from 0 to  $2e^2/h$  takes place, which indicates a quantization of the Hall conductance and an occurring of a phase transition at  $M=M_c$ . After that, it remains  $2e^2/h$ , in which the unstrained graphene stays in the phase of QAHE. Furthermore, the applied strain drives Hall conductance curve forward to the right-hand side for strained graphene. Consequently, as the strain modulus increases from zero, the critical exchange field  $M_c$  becomes larger, such as for  $\varepsilon=0.2$ ,  $M_c=0.275t$  with a relative change of  $M_c$  being approximately +14.5%. Astonishingly, in the case of  $\theta=0$ , as demonstrated in **Figure 10(c)**, there is an increase in the exchange field with similar behavior for the Hall conductance. However, beyond an specific value of strain modulus, indicated by the vertical dashed line in **Figure 10(e)**, the system presents an opposite strain-strength dependence, i.e., an increase in the strain parameter shifts the Hall conductance curve to the left-hand side. For instance, in the case of  $\varepsilon=0.2$ , we have obtained  $M_c=0.1t$  with a relative change of  $M_c$  being equal to -58.3%.

The distinct behaviors observed along different strain directions for the QAHE phase transition can be explained by the competition of the Rashba SOC and ISO in the bulk band gap-closing phenomena for a given critical exchange field  $M_c$  [31, 45]. In the case of  $\theta=\pi/2$ , an increase in the strain modulus leads to an approximately linear enhancement in the ISO parameter as can be observed in **Figure 10(e)**, which results in a smaller bulk band gap in the presence of an exchange field. On the other hand, the Rashba SOC is not very sensitive to the variation of strain strength. Therefore, the variation of Hall conductance mainly reflects the dependence of ISO on the strain strength. In contrast, for values of strain modulus larger than  $\varepsilon=0.078$  in the case of  $\theta=0$ , there is drastic reduction in the effective ISO interaction, hence Rashba becomes dominant and the critical exchange field for the phase transition becomes smaller as one can note in **Figure 10(c)** with a critical  $M_c=0.1t$  for  $\varepsilon=0.2$  for the QAHE phase transition [32].

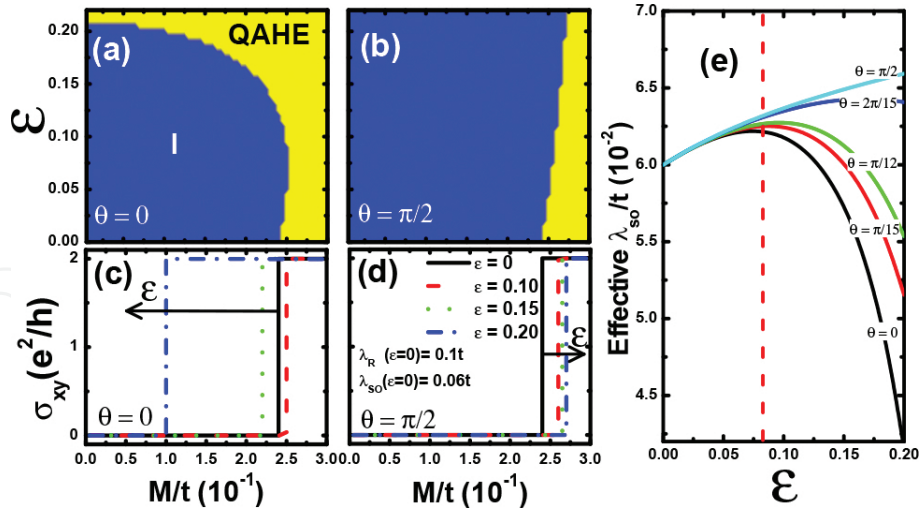


**Figure 10.** Phase diagram of the QAHE for strained graphene along two distinct directions: (a) along  $\theta=0$  and (b) along  $\theta=\pi/2$ . The Hall conductance as a function of the exchange interaction  $M$ , for uniaxial strain direction along  $\theta=0$  and  $\theta=\pi/2$  with four different strain strengths is shown in (c) and (d), respectively. The arrows in panels (c) and (d) indicate the direction for which the strength is increased from  $\varepsilon=0$  to  $\varepsilon=0.2$ . The parameters  $\lambda_R(\varepsilon=0)=0.1t$  and  $\lambda_{so}(\varepsilon=0)=0.06t$  have been used in panels (a)–(d). (e) Effective  $\lambda_{so}$  as function of strain strength along different directions  $\theta$ . The vertical dashed line in panel (e) indicates the limiting strain modulus, for which the effective ISO parameter changes its behavior according to the direction and modulus of strain. Reproduced with permission from Diniz et al. [32]. Copyright (2013), AIP Publishing LLC.

### 3. Electronic structure and transport properties of graphene nanoribbon

A graphene nanoribbon is defined as a graphene sheet in which one of its dimensions is narrow and the other approximately infinite. The unique properties arising due to the reduced dimensions become very important because shape of the edges and width of nanoribbon defines its electronic structure. The main nanoribbons classification is based on the edge design, which can be armchair, zigzag, chiral, and bearded nanoribbons depending on the edge terminations [82]. We will focus on the electronic dispersion of only two types: armchair and zigzag.

#### 3.1. Electronic structure of graphene nanoribbon

The electron wave function in a armchair nanoribbon is

$$|\phi_{A,n}\rangle = \frac{1}{\sqrt{M}} \sum_{m,n} e^{ik \cdot \vec{R}_m} |A_m, n\rangle \quad (47)$$

where

$$\vec{R}_m = m\vec{a}_0 \quad (48)$$

is a vector between the atom and its neighbors in the next unit cell with same type of site. In armchair nanoribbons, the unit cell  $m$  and its width is defined as shown in **Figure 11(a)**. One can write the vectors that separate the nearest neighbors for a A site, **Figure 11(b)**:

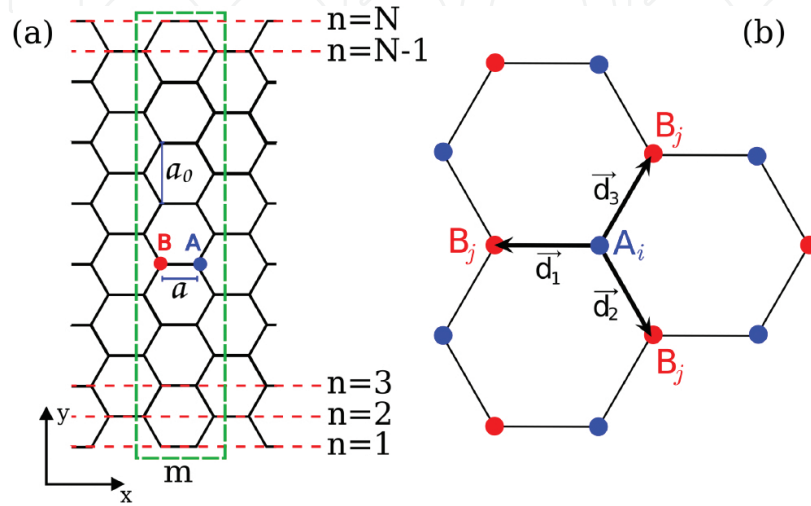


**Figure 11.** (a) Armchair unit cell  $m$  showing the sites A and B, distance between carbon atom  $a$  and lattice constant  $a_0$  is also shown. (b) Distance vectors between two nearest neighbors sites and site index.

$$\vec{d}_1 = -a\hat{i} \quad (49)$$

$$\vec{d}_2 = \frac{a}{2}\hat{i} - \frac{a_0}{2}\hat{j} \quad (50)$$

$$\vec{d}_3 = \frac{a}{2}\hat{i} + \frac{a_0}{2}\hat{j} \quad (51)$$

And similar vectors could be find for B sites. Then, Hamiltonian of armchair nanoribbon is

$$\hat{H}_h = - \sum_{\langle m,n \rangle}^N \{ t_1 |A_m, n\rangle \langle B_{m-1/2}, n| + t_2 |A_m, n\rangle \langle B_m, n-1| + t_3 |A_m, n\rangle \langle B_m, n+1| + h.c \} \quad (52)$$

where the summation  $\langle m,n \rangle$  is over nearest neighbors; the product  $|a_m, n\rangle \langle B_{m-1/2}, n|$  is the hopping of electrons between an atom in the A site at position  $m$  and  $n$  and an atom in

neighboring site B which is at position  $m - \frac{1}{2}$  and  $n$ . Solving Schrödinger's equation will give energy expressions

$$E\alpha(\vec{k}, n) = -t \left[ \beta(\vec{k}, n)e^{-ik_x a_0/2} + \beta(\vec{k}, n+1) + \beta(\vec{k}, n-1) \right] \tag{53}$$

$$E\beta(\vec{k}, n) = -t \left[ \alpha(\vec{k}, n)e^{ik_x a_0/2} + \alpha(\vec{k}, n+1) + \alpha(\vec{k}, n-1) \right] \tag{54}$$

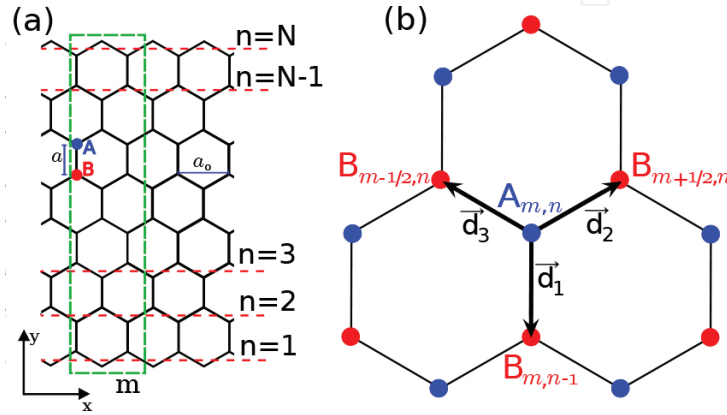


**Figure 12.** (a)  $m$ th unit cell of zigzag graphene ribbon, and (b) distance vectors between two nearest neighbor sites and index of them. In (a), A and B indicate two sites,  $a$  is interatomic distance, and  $a_0$  represents lattice constant.

Zigzag nanoribbon has unit cell  $m$  and width defined as showed in **Figure 12(a)**. The vectors that separate the nearest neighbors for a A site, **Figure 12(b)**, are the same as the graphene case. The Hamiltonian is

$$H = -\sum_{m,n}^N \{ t_1 | A_m, n \rangle \langle B_m, n-1 | + t_2 | A_m, n \rangle \langle B_{m+1/2}, n | + t_3 | A_m, n \rangle \langle B_{m-1/2}, n | + h.c \} \tag{55}$$

Now, the energies are

$$E\alpha(\vec{k}, n) = -t \left[ \beta(\vec{k}, n)2\cos\left(\frac{k_x a_0}{2}\right) + \beta(\vec{k}, n-1) \right] \tag{56}$$

$$E\beta(\vec{k}, n) = -t \left[ \alpha(\vec{k}, n)2\cos\left(\frac{k_x a_0}{2}\right) + \alpha(\vec{k}, n+1) \right] \tag{57}$$

and energy dispersion for a  $N = 24$  zigzag nanoribbon can be seen in **Figure 13**, where the edge states are marked blue and gray lines denotes bulk states. In **Figure 14**, intrinsic spin-orbit is applied with  $\lambda_{so} = 0.05t$ . The electronic density is very localized near the edges of the nanoribbon, **Figure 14(b)**.

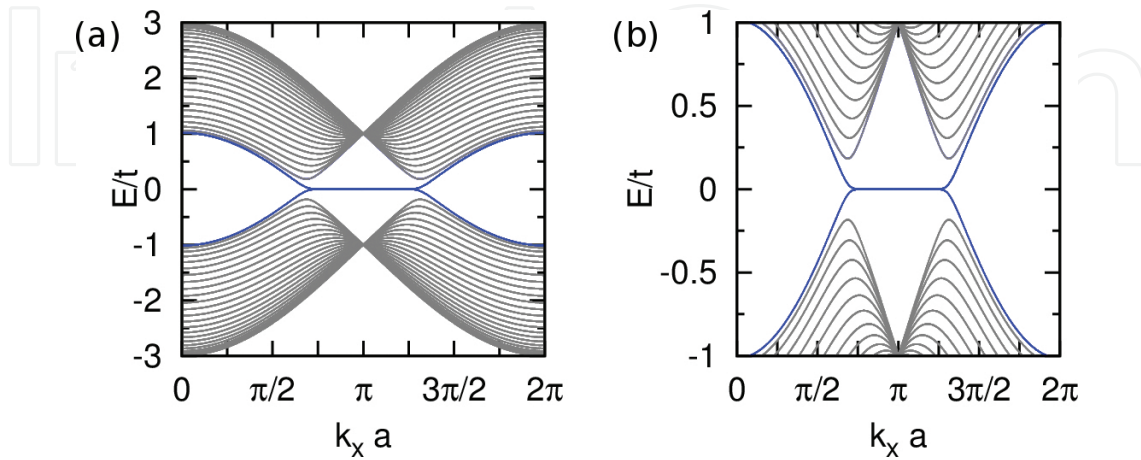


**Figure 13.** Energy band of bulk- (gray lines) and edge- (blue lines) states of zigzag nanoribbon with width  $N = 24$ .

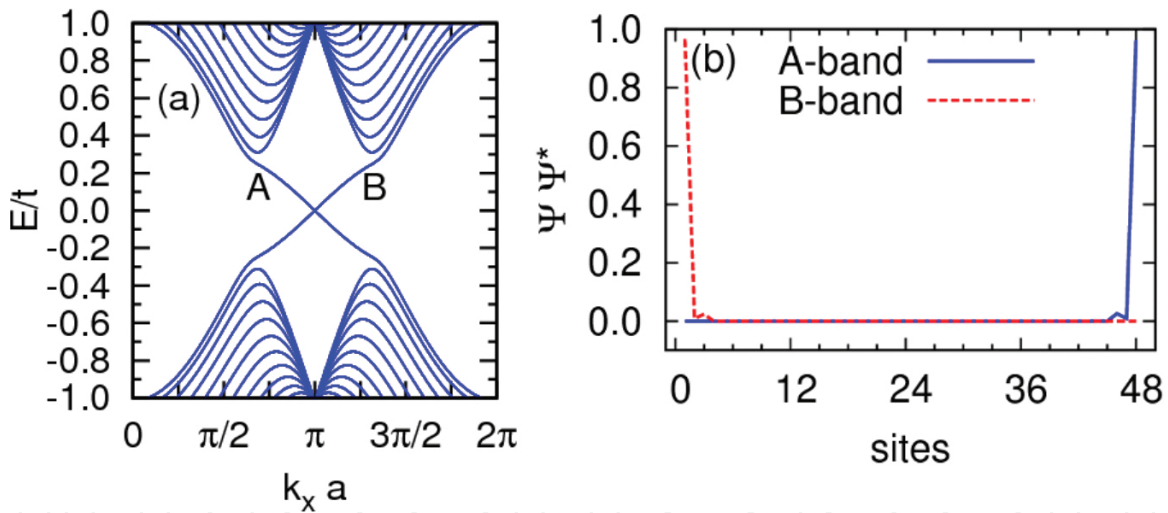


**Figure 14.** (a) Energy band of zigzag nanoribbons with  $N = 24$  and  $\lambda_{so} = 0.05t$ , and (b) electronic probabilities of A- and B-edge states defined by cross points between edge states and Fermi level  $E = 0.05t$ , as indicated in (a).

*Electronic structure of strained graphene nanoribbon*-For the case of strained graphene nanoribbons, we need to replace the strain-invariant hopping integrals by the strain-dependent ones [52, 83] as described in Section 2.2. Many interesting properties are observed in the optical conductivity [72] and electronic transport [84, 85] when the uniaxial strain is considering in the graphene nanoribbons. In the next section, we discuss in detail the effects of uniaxial strain in the spin-charge electronic transport and QAH effect.

### 3.2. Transport properties of strained graphene nanoribbon

Here, we aim to analyze the electronic transport control in GNR with different terminations in the QAH phase by means of uniform strain deformations [86]. The electronic transport can be performed using a two-terminal device akin to a field electron transistor (FET). QAH phase can be determined experimentally, by spin-resolved density of states, that can be accessed by spatially scanning tunneling microscope (STM) or by scanning tunneling spectroscopy (STS) [87–89]. To calculate the spin-resolved conductance, we have implemented the standard surface Green's function approach [90, 91]. The GNR device is divided into three regions: left lead, central conductor, and right lead. The uniaxial strain is applied to either the longitudinal ( $\theta=0$ ) or the transversal ( $\theta=\pi/2$ ). The central conductor is the only region under the influence of SOC effects and exchange field; it is also connected to semi-infinite leads by nearest-neighbor hopping. To avoid surface mismatch in the case of strained GNR [85], we have considered that the leads are also strained. Therefore, a perfect atomic matching at the interface leads/central conductor is achieved. The Green's function of the device (omitting the spin indices) is then calculated by

$$\mathcal{G}_C^{a/r}(E) = (E \pm i\eta - H_C - \Sigma_L - \Sigma_R)^{-1}, \quad (58)$$

where  $a/r$  denotes the advanced/retarded Green's function,  $E$  is the energy ( $\eta \rightarrow 0$ ) of the injected electron (the Fermi energy at a given doping).  $H_C$  stands for the Hamiltonian in the central region, and  $\Sigma_{L/R}$  are the self-energies that describe the influence of the left/right leads,  $\Sigma_l = H_{lC}^\dagger g_l H_{lC}$ , where  $g_l$  is the Green's function for the  $l=L, R$  semi-infinite lead obtained through an iterative procedure of the tight-binding Hamiltonian [90], and  $H_{lC}$  couples each lead to the central region. The spin resolved conductance through the system is given by [86],

$$G_{\sigma\sigma'} = G_0 \text{Tr} \left[ \Gamma_\sigma^L \mathcal{G}_{C,\sigma\sigma'}^r \Gamma_{\sigma'}^R \mathcal{G}_{C,\sigma\sigma'}^a \right], \quad (59)$$

where the trace runs through the lattice sites at the central conductor,  $G_0 = e^2/h$  is the quantum of conductance per spin, and  $\Gamma_\sigma^l$  are the couplings for the leads, related to the spin-diagonal self-energies by  $\Gamma^l = i[\Sigma_l^r - \Sigma_l^a]$  [90].

To study the conductance characteristics in the presence of both Rashba SOC and exchange field [86], we set the parameters  $\lambda_R = 0.1t_0$ ,  $M = 0.2t_0$ , and  $\lambda_{so} = 0t_0$ . Notice that with these parameters, the system is in the QAH phase [31]. Nevertheless, if the ISO parameter is different from zero, there is an upper-limited value of  $\lambda_{so}$  [31, 32], beyond which a new phase characterized by a vanishing Chern Number  $C=0$  can take place; this phase is the so-called TRS-broken QSH phase [31, 32, 34]. The spin-resolved conductance  $G_{\sigma\sigma'}$  is shown in **Figure 15**: for (a) unstrained, (b) strained along  $\theta=0$ , (c) strained along  $\theta=\pi/2$ , and (d) the total conductance  $\sum_{\sigma\sigma'} G_{\sigma\sigma'}$  of a ZGNR. Notice that there is a suppression for both the spin conserving and the spin-flip

conductance components for either unstrained or strained ZGNR in the energy range considered. However, these backscattering (transmission dips) at certain precise energies at the first plateau are different depending on the strain configuration, and a close inspection shows that conducting channels for non-spin flip and spin-flip conductances oscillate. Depending on the Fermi energy and set parameters, certain conductance components can even be completely suppressed. This suppression is attributed to the appearance of quasi-localized states in the device, which may produce sharp scattering resonances, also known as resonant backscattering which is a general behavior of quasi-1D quantum systems [92]. For higher energies, however, the large number of conducting channels leads to a nonvanishing transmission, as the channels get mixed along the device and results in the appearance of an interchannel backscattering leaded by interference effects. Therefore, in the QSH phase protected by the TRS, nonmagnetic impurities do not cause backscattering on each boundary, and the spin transport in the edge states is dissipationless at zero temperature.

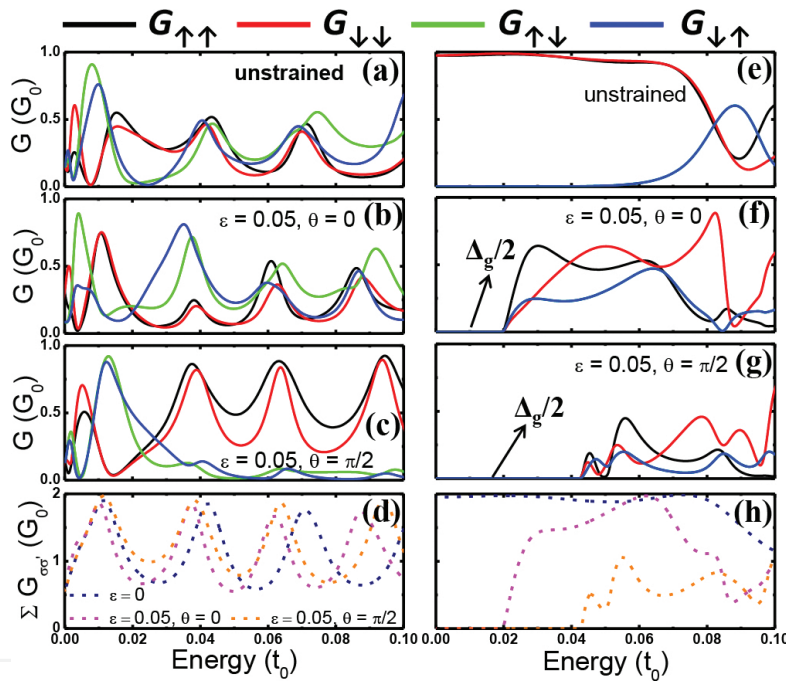


**Figure 15.** Effects of strain on spin-resolved conductance  $G_{\sigma\sigma}$  of ZGNR with  $N_Z=26$  (a)–(c) and AGNR with  $N_A=47$  (e)–(g), respectively. Panels (d) and (h) show the total conductance. The parameters used in all panels are  $\lambda_R=0.1t_0$ ,  $\lambda_{so}=0$ , and  $M=0.2t_0$ . Reproduced with permission from Diniz et al. [86]. Copyright (2014), AIP Publishing LLC.

In the QAH phase, however, there is a weak scattering between forward and backward movers, leading to a low-dissipation spin transport. At low energy, this interesting strain-controllable behavior of conducting channel suppression might be efficiently used to filter electrical current of desired spins, in spin filtering devices [86]. In **Figure 15(d)**, we show the total conductance, which is nearly robust against strains, specially close to the charge neutrality point, where the deviations due to strain are quite small. In contrast, the conductance of AGNR shows a drastic modification as one can notice in **Figure 15(e)–(h)**, with the development of a

transport gap, which is insensitive to the electron spin that is injected and collected in the device. However, this induced transport gap is dependent upon the direction of the applied strain, with a larger conduction suppression along  $\theta=0$  (red dashed line) with  $\Delta_g = 0.04 t_0$ , and  $\Delta_g = 0.086 t_0$  while along  $\theta=\pi/2$ , that can be observed in **Figure 15(h)**. Also, the total conductance exhibits different plateaus: around  $2G_0$  and approximately  $G_0$  in AGNR without and with strain, respectively, which is one less quantum of conductance available for the electron to be transmitted along the strained device for energies beyond the transport gap.

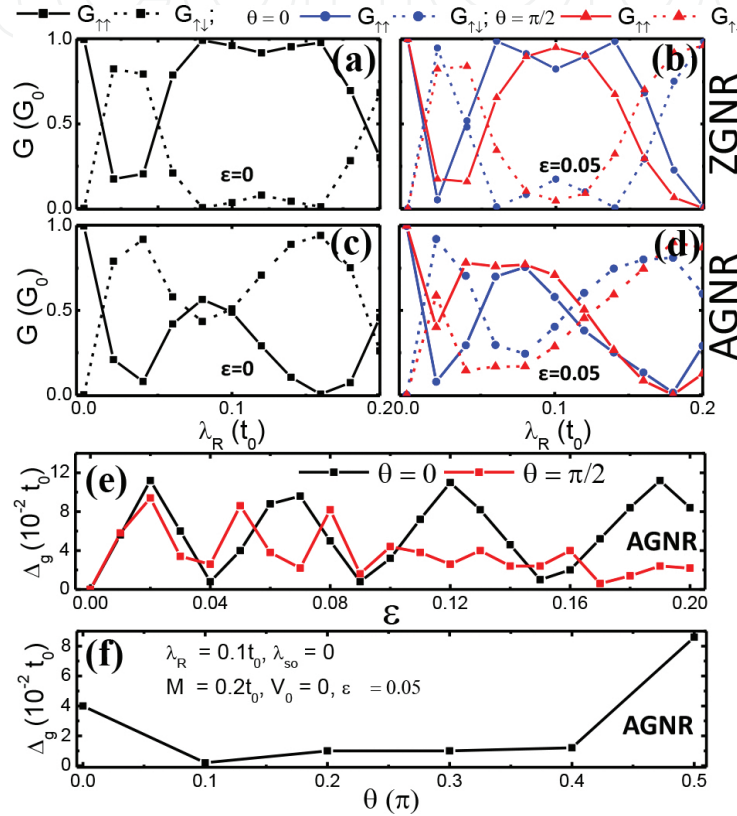


**Figure 16.** (a) Conductance profiles  $G_{\uparrow\uparrow}$  and  $G_{\uparrow\downarrow}$  for 26-ZGNR (a)–(b) and 47-AGNR (c)–(d) as function of  $\lambda_R$  subjected to different configurations of strain. Panels (e) shows the band gap  $\Delta_g$  of an AGNR as function of strain parameter  $\epsilon$  for  $\theta=0$  and  $\theta=\pi/2$ , respectively. (f)  $\Delta_g$  of an AGNR as function of the direction of strain for fixed  $\epsilon=0.05$ . Reproduced with permission from Diniz et al. [86]. Copyright [2014], AIP Publishing LLC.

Another remarkable phenomenon is the oscillatory dependence of the spin components of  $G_{\sigma\sigma}$  on the value of  $\lambda_R$  [86], which is shown in **Figure 16(a)–(d)**, where the curves correspond to different topological GNRs and strain setups for  $E=0.05t_0$ . The same parameters are used as the **Figure 15**, except for  $M$ . To reveal the effects of Rashba SOC, we set  $M=0$  in the calculation. Then, the system is time-reversal invariant and the conductance components  $G_{\uparrow\uparrow}=G_{\downarrow\downarrow}$  and  $G_{\uparrow\downarrow}=G_{\downarrow\uparrow}$ . This oscillatory behavior is reminiscent of the spin field effect transistor (FET) and has a similar source [93], as the spin *precesses* as it propagates in the presence of the Rashba field, acquiring a net phase that is proportional to  $\lambda_R L$ , where  $L$  is the length of the device.

Further inspecting the strain-induced band gap in 47-AGNR in the presence of SOC and exchange field interactions, one notices that in **Figure 16(e)** a similar band gap oscillation characteristic as reported in a earlier work [84]. In the regime of small strain, the band gap shows approximately linear response, with increasing values of strain, however, it starts to oscillate. Further investigation shows that the amplitude and period of the gap oscillation are tuned by direction of the strain, as shown in **Figure 16(e)**. A specific dependence of transport gap on the angle of the strain is clearly depicted in **Figure 16(f)**. Notice that the transport gap is indeed strongly tuned by strain direction. It equals approximately zero at  $0.1\pi$ , while it reaches  $0.086 t_0$  at  $0.5\pi$ .

### 3.3. Quantum phase transitions in strained graphene nanoribbon

Quantum spin Hall and quantum anomalous Hall (QAH) states have topologically protected edge states, where the electron back scattering is forbidden, making these systems good candidates for electronic devices with dissipationless electronic transport [33, 35, 38, 41]. The potential possibility to explore the different Quantum Hall phases in strained graphene has motivated us to study the strain-related physics at zero magnetic field in graphene nanoribbons [49].

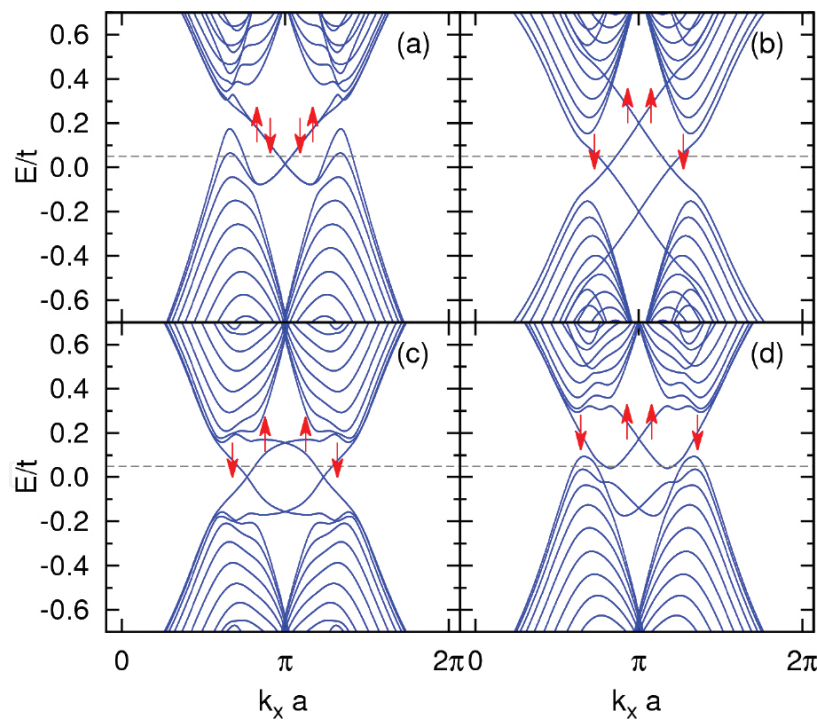


**Figure 17.** Energy band of ZGNR with intrinsic- and Rashba-SOC terms (a), intrinsic SOC and EX (b), Rashba SOC and EX (c), and intrinsic- and Rashba-SOCs and EX (d). The Fermi level is assumed to be above zero, as indicated by the dashed horizontal line, and thus has four intersections with the conduction bands. This gives rise to four edge currents on the ribbon edges. The following parameters are used: (a)  $\lambda_{so}=0.06t$ ,  $\lambda_R=0.20t$ ; (b)  $\lambda_{so}=0.06t$ ,  $M=0.20t$ ; (c)  $\lambda_R=0.20t$ ,  $M=0.20t$ ; (d)  $\lambda_{so}=0.06t$ ,  $\lambda_R=0.20t$ , and  $M=0.20t$  for the ZGNR with width  $W=48$ . The arrows represent the major components of spin. Copyright (2015) by the American Physical Society [49].

If the mirror symmetry about the graphene plane is preserved, then the intrinsic SOC which opens gaps around Dirac points is the only allowed spin-dependent term in the Hamiltonian. Otherwise, if the mirror symmetry is broken, then a Rashba term is allowed, which mixes spin-up and spin-down states around the band crossing points. Besides, Rashba SOC pushes the valence band up and the conduction band down, reducing the bulk gap. Following Reference [45], we present our results for the ZGNR in **Figure 17**, which shows the effects of intrinsic and Rashba-SOCs and EX upon the energy band of the ZGNR [49]. Notice in **Figure 17(a)** that the interplay between intrinsic- and Rashba-SOCs partially lifts the degeneracies of both bulk- and edge-state, breaks particle-hole symmetry and pushes the valence band up. In turn, the presence of the EX breaks the TRS and lifts the Kramer's degeneracy of electron spin, pushing the spin-up (spin-down) bands upward (downward), as shown in **Figure 17(b)**. In strong contrast with **Figure 17(b)**, the presence of Rashba SOC and EX induces coupling between edge and bulk states, which significantly modifies the group velocity of edge states, as shown in **Figure 17(c)**. The combined effects of intrinsic, Rashba SOC and EX are shown in **Figure 17(d)**, which are in agreement with results reported in Reference [45] (see for instance **Figure 2**). Notice that the Fermi level enters into the valence band and the energies of some edge modes are smaller than the valence band maximum.

The intrinsic SOC can be strongly enhanced by impurity (adatom) coverage on the surface of graphene, which produces strong lattice distortions [59]. In this context, one may ask how the quantum phase transition in a graphene ribbon changes as the intrinsic SOC is tuned [49]. Following the discussion of Reference [45], the effects of strain fields are shown in **Figure 18** (with a similar representation to the one introduced in Reference [45]) with parameters  $W=48$ ,  $\lambda_R=0.20t$ ,  $M=0.20t$ , and uniaxial strain  $\varepsilon=0.10$  along  $\theta=0$ . The left panel of **Figure 18** shows the effects of intrinsic SOC on the energy spectrum of a ZGNR. The Fermi level is set at  $E_F=0.05t$ . The corresponding edge state probability distributions across the width of the nanoribbon, for each of the four edge states indicated by A, B, C, and D, are shown in the middle panel. Schematic diagrams of charge current distributions on the edges of ZGNR are illustrated in the right panel. To determine the edge current direction,  $I = -|e|v_x$  (indicated by the arrow), the electron group velocity  $v_x = \partial E(k) / \partial k_x$  has been calculated [45]. In the case of weak intrinsic SOC, at the ribbon boundaries, the edge states pair A and D would form a single handed loop (in the sense that the turning point is at infinity along the ribbon length), meanwhile there is the formation of another loop with opposite handedness, which is formed by the edge states pair B and C. Both edge states A and B, consequently  $I_A$  and  $I_B$ , are located at the same edge, as indicated in **Figure 18(c)**. Thus, the chirality of the current loop due to the A and D edge states would produce a Chern number of  $(C_1 = \pm 1)$ , which is the same as that of current loop owing to B and C edge states. Since the system is akin to two integer quantum Hall subsystems, its Chern number  $(C)$  is equal to  $(C_1 = +1) \oplus (C_2 = +1)$ , i.e.,  $C = (+1) + (+1) = 2$  or  $(C_1 = -1) \oplus (C_2 = -1)$ , with  $C = (-1) + (-1) = -2$ . Therefore, the ZGNR with a weak intrinsic SOC is in the QAH phase. For a ZGNR with strong intrinsic SOC, however, one can notice that the edge states pair A and C are located on the same edge, whereas the B and D edge states are in the opposite edge, as shown in **Figure 18(f)**. Due to the handedness of the current loop of edge

states A and D, the Chern number would give a contribution of ( $C_1 = -1$ ), and the pair B and C, which has an opposite handedness, produces a Chern number of ( $C_2 = +1$ ). Since the ZGNR is composed of these two integer quantum Hall subsystems, its Chern number ( $C$ ) is obtained by ( $C_1 = +1$ ) $\oplus$ ( $C_2 = -1$ ), i.e.,  $C = (+1) + (-1) = 0$ . Therefore, the GNR is in the TRS broken QSH phase.

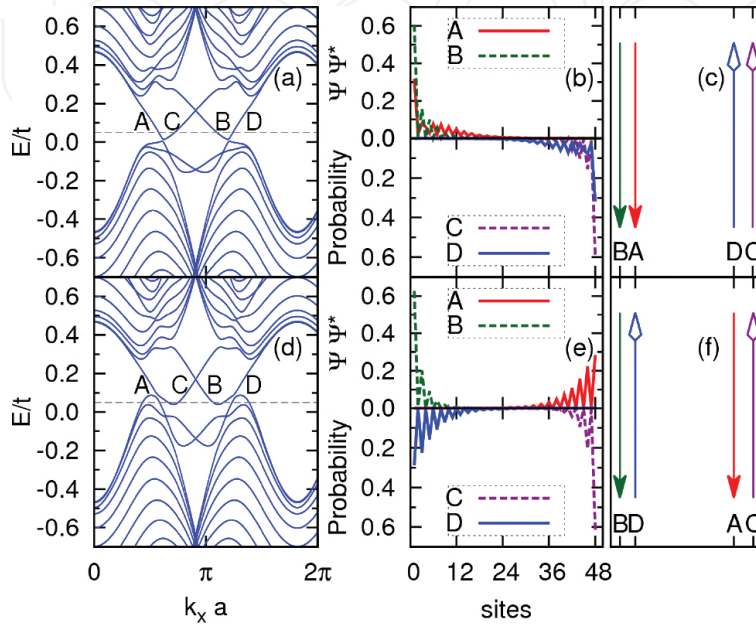


**Figure 18.** Energy spectrum of ZGNR with  $W = 48$ ,  $\lambda_R = 0.20t$ ,  $M = 0.20t$ ,  $\varepsilon = 0.10$ , and  $\theta = 0$ , for (a)  $\lambda_{so} = 0.035t$  and (d)  $\lambda_{so} = 0.055t$ , respectively. The Fermi level  $E = 0.05t$  corresponds to four different edge states, as indicated by A, B, C, and D. The corresponding probability distributions  $|\psi|^2$  across the width of the ribbon, and diagrams of charge current distributions are shown in the middle (b)–(e) and right panels (c)–(f), respectively. The arrows indicate the current flux. Copyright (2015) by the American Physical Society [49].

To understand the QPT and show intuitively how it takes place [49], we follow Reference [45] and introduce the average value of the position  $\langle y \rangle_n$ , as a parameter to label the angular momentum of the current [49]. It is defined as:  $\langle y \rangle_n = \sum_i y_i |\varphi_n(y_i)|^2$ , where  $n$  represents the edge states at the Fermi level and  $i$  is the site index along the width of ribbon. We chose the origin of  $y$  axis at the lower boundary of the ribbon. **Figure 19(a)** shows the average values  $\langle y \rangle_n$  of edge states as a function of  $\lambda_{so}$  in the ribbon with the width  $W = 48$ ,  $\lambda_R = 0.20t$ ,  $M = 0.20t$ ,  $\varepsilon = 0.10$ , and  $\theta = 0$ , where  $n = A, B, C$ , and  $D$ , respectively. The direction and magnitude of a group velocity are indicated by the direction and length of an arrow, respectively. When the intrinsic SOC is vanishing, the Rashba SOC and EX are dominant, A and B are on the same boundary of the ribbon, and thus both  $\langle y \rangle_A$  and  $\langle y \rangle_B \rightarrow 0$ . The edge states C and D also follow the same behavior, but are localized at the other edge of the ribbon, thus  $\langle y \rangle_C$  and  $\langle y \rangle_D \rightarrow W$ . The system is in the QAH phase. When the  $\lambda_{so}$  increases, however, three different topological phases are found. In the regime of small  $\lambda_{so}$  ( $0.03t < \lambda_{so} < 0.04t$ ), the positions of the edge states are only very

slightly shifted. With increasing  $\lambda_{so}$ , the states A and D become delocalized, swiftly moving to the center of the ribbon from different boundaries owing to the edge- and bulk-states coupling. In the regime of large  $\lambda_{so}$  ( $\lambda_{so} > 0.05$ ), the locations of state A and D have been exchanged. Since the group velocity of state A is opposite to D, the exchange of their locations results in a change of chirality. Therefore, the system is in the QSH phase. It is worthy to point out that owing to the finite-size (finite-width) effect, the edge states are not exactly localized at the two boundaries. Remarkably, a similar behavior is also presented in **Figure 19(b)** in which  $\langle y \rangle$  versus strain is plotted. At first glance, it seems to be hard to understand this exotic behavior. But, recalling the discussion of phase transition in bulk graphene, one can logically speculate that this is a manifestation of strain-induced QPT between QSH and QAH states in the ZGNR. This strain-induced QSH state shares many emergent properties similar to the usual zero-strain QSH effect. We notice that with realistic values for uniaxial strain the critical value for the spin-orbit coupling is reduced by a factor between 10% and 20%. Thus, the combination of strain and appropriate substrates shows a promising direction to realize the phase transition in current settings.

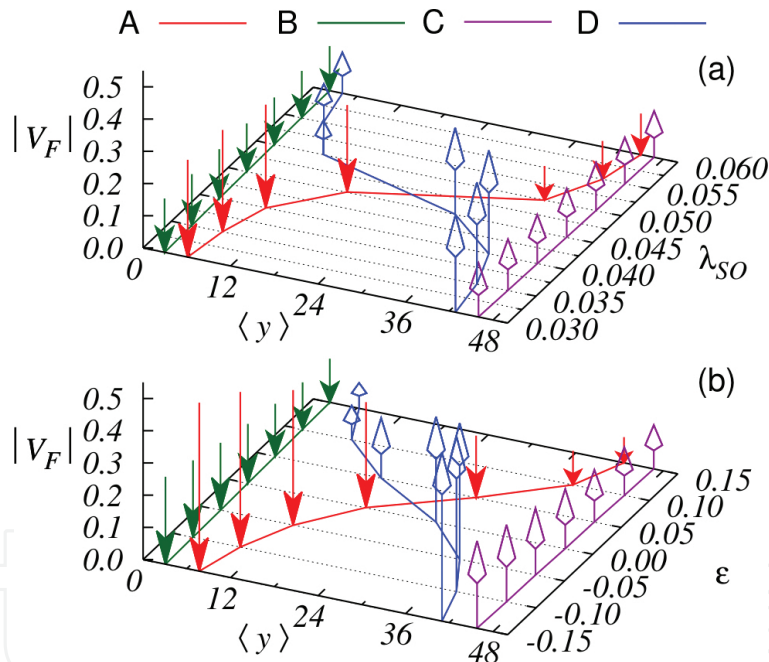


**Figure 19.** (a) Average values  $\langle y \rangle$  of edge states versus  $\lambda_{so}$  in ZGNR, subjected to a strain with  $\epsilon = 0.10$  and  $\theta = 0$ . (b)  $\langle y \rangle$  as a function of strain with  $\theta = 0$  for  $\lambda_{so} = 0.05t$ .  $W = 48$ ,  $\lambda_R = 0.20t$ , and  $M = 0.20t$  are used in the computations. Vertical axis is the Fermi velocity  $V_F$  modulus. The arrows point in the directions of band velocities and their lengths present the magnitudes of  $V_F$ . Copyright (2015) by the American Physical Society [49].

To seek the controllable topological QPTs induced either by strain (EX), or intrinsic SOC, or any of their combinations [49], the phase diagrams in which the phase is characterized by the difference in the average value of position  $\langle y \rangle_C$  and  $\langle y \rangle_{A'}$ , defined as  $\langle y \rangle_{AC} = \langle y \rangle_C - \langle y \rangle_{A'}$ , are constructed, as shown in **Figure 20**. **Figure 20(a)** and **(b)** plots the phase diagrams of  $\epsilon$  versus

$\lambda_{so}$  for  $\theta=0$  and  $\theta=\pi/2$ , respectively. It is trivial to notice that if  $\langle y \rangle_{AC} \cong 0$ , the edge states A and C are localized at the same boundary, corresponding to a QSH phase, as indicated by blue. Otherwise, if  $\langle y \rangle_{AC} \cong W$ , the system is in the QAH phase, as marked by red. The other values of  $\langle y \rangle_{AC}$  correspond to delocalized state A. Notice that both strength and direction of the strain change considerably the phase diagram. In the regime of small intrinsic SOC, the GNR lies in the QAH state. The critical  $\lambda_{so}^c$  at which topological QPT depends strongly on both the strength and direction of the strain. The larger the strain, the smaller the  $\lambda_{so}^c$  is required to reach the QSH state. In addition, the strain drives the GNR from the QAH into QSH states for a given  $\lambda_{so}^c$ . It is also noted that in the case of  $\theta=\pi/2$ , when the  $\lambda_{so}^c$  changes in the boundary between the QSH and QAH states, the correspondent critical value of  $\varepsilon$  varies faster than that for  $\theta=0$ .

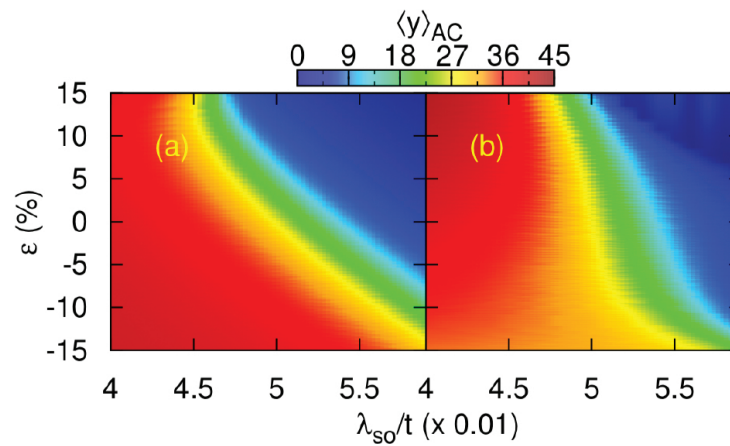


**Figure 20.** Phase diagrams (strain vs. intrinsic SOC) of a ribbon with  $W=48$ ,  $\lambda_R=0.20t$ , and  $M=0.20t$ , characterized by a difference in the average value of position between mode A and C, defined as  $\langle y \rangle_{AC} = \langle y \rangle_C - \langle y \rangle_A$ , for  $\theta=0$  (a) and  $\theta=\pi/2$  (b), respectively. Copyright (2015) by the American Physical Society [49].

The underlying physics of the strain tuned phase diagram is as follows. It is well established that uniaxial mechanical strain does not break the sublattice symmetry, but rather deforms the Brillouin zone, such as, the Dirac cones located in graphene at points  $K$  ( $K'$ ) being shifted in the opposite directions [52, 83]. This is reminiscent of the effect of pseudomagnetic field  $B_S$  induced by the strain on charge carriers, i.e., accumulating charge in place where the  $B_S$  is maximum. Because the  $B_S$  does not break TRS, the strain will not have any direct effect on the spin degrees of freedom of the electrons, even though it couples with sublattice pseudospin. Therefore, at first glance, it seems that the strain only induces a renormalization of the energy scales. Actually, *this is not true* for graphene with SOC. Since SOC couples the spin and the momentum degrees of freedom of the carriers,  $B_S$  could affect real spin of an electron through the SOC. Therefore, a strong pseudomagnetic field should lead to Landau quantization and a QSH state due to opposite signs of  $B_S$  for electrons in valleys  $K$  ( $K'$ ). In this context, the strain enhances the carrier localization and pushes the edge states much closer to the boundaries of

the ribbon. Hence, the QSH state could be stabilized by the strain. Finally, it is worthwhile to argue that since inter-valley scattering requires a large momentum transfer [94], it is strongly suppressed in wide ZGNRs in which we are interested.

## 4. Conclusion

In summary, we have performed a systematic investigation of the effects of uniaxial strains, exchange field, staggered sublattice potential, and SOC on the electronic and transport properties of graphene and graphene nanoribbons. We have employed the tight-binding approximation, and Green's function formalism in order to fully describe the electronic and transport properties of these interesting nanostructures.

Using an effective low energy approximation, we were able to describe the Berry curvature and the associated Chern numbers for different orientation and uniaxial strain strength, as function of exchange field interaction. The QSH–QAH phase transition associated to the tunability of Chern number for the bulk graphene displays an interesting behavior according to specific directions of strains: an increase in the critical exchange field  $M_c$  for the QAHE phase transition for  $\theta=\pi/2$  as the strain modulus is enhanced, in contrast to the  $\theta=0$ , which shows a reduction (above a limiting strain modulus of approximately  $\varepsilon=0.078$ ) in the critical exchange field  $M_c$  for the QAHE phase [32]. The investigated spin-resolved electronic transport and LDOS of GNR devices have demonstrate that it is possible to achieve a total electron transmission suppression of specific spin specie, which can be further tailored by uniaxial tensile strain on specific directions [86]. In addition, we have implemented a formalism to describe the zero-field topological QPT between QSH and QAH states in GNRs in the presence of internal EX, uniaxial strain, and intrinsic and Rashba SOCs [49].

Our results demonstrated in this Chapter offer the prospect to efficiently manipulate the electronic structure, transport properties, and consequently the QAHE by strain engineering of the graphene. We also envision that our work can be extended to other layered materials (for instance, transition metal dichalcogenides), with a great potential application on novel electronic devices with the focus on dissipationless charge current.

## Author details

Fanyao Qu<sup>1\*</sup>, Ginetom S. Diniz<sup>2,3</sup> and Marcos R. Guassi<sup>1</sup>

\*Address all correspondence to: fanyao@unb.br

1 Institute of Physics, University of Brasília, Brasília, DF, Brazil

2 Institute of Physics, Federal University of Uberlândia, Uberlândia, MG, Brazil

3 Institute of Science and Technology, Federal University of Goiás, Jataí, GO, Brazil

## References

- [1] R. E. Peierls. Quelques proprietes typiques des corps solides. *Ann. I. H. Poincare*, 5:177, 1935.
- [2] L. D. Landau. Zur theorie der phasenumwandlungen ii. *Phys. Z. Sowjetunion*, 11:26, 1937.
- [3] J. A. Venables, G. D. T. Spiller, and M. Hanbucken. Nucleation and growth of thin films. *Rep. Prog. Phys.*, 47:399, 1984.
- [4] J. W. Evans, P. A. Thiel, and M. C. Bartelt. Morphological evolution during epitaxial thin film growth: Formation of 2D islands and 3D mounds. *Sur. Sci. Rep.*, 61:1, 2006.
- [5] P. R. Wallace. The band theory of graphite. *Phys. Rev.*, 71:622–634, 1947.
- [6] K. S. Novoselov, A. K. Geim, S. V. Morozov, D. Jiang, Y. Zhang, S. V. Dubonos, I. V. Grigorieva, and A. A. Firsov. Electric field effect in atomically thin carbon films. *Science*, 306(5696):666–669, 2004.
- [7] A. K. Geim and K. S. Novoselov. The rise of graphene. *Nature materials*, 6(3):183–191, 2007.
- [8] J. L. Tedesco, B. L. VanMil, R. L. Myers-Ward, J. M. McCrate, S. A. Kitt, P. M. Campbell, G. G. Jernigan, J. C. Culbertson, C. R. Eddy Jr, and D. K. Gaskill. Hall effect mobility of epitaxial graphene grown on silicon carbide. *Appl. Phys. Lett.*, 95(12):122102, 2009.
- [9] T. Shen, J. J. Gu, M. Xu, Y. Q. Wu, M. L. Bolen, M. A. Capano, L. W. Engel, and P. D. Ye. Observation of quantum-hall effect in gated epitaxial graphene grown on SiC (0001). *Appl. Phys. Lett.*, 95(17):172105, 2009.
- [10] J. Hass, F. Varchon, J. Millan-Otoya, M. Sprinkle, N. Sharma, W. A. de Heer, C. Berger, P. N. First, L. Magaud, and E. H. Conrad. Why multilayer graphene on 4 h-sic (000 1 $\bar{1}$ ) behaves like a single sheet of graphene. *Phys. Rev. Lett.*, 100(12):125504, 2008.
- [11] G. M. Rutter, J. N. Crain, N. P. Guisinger, T. Li, P. N. First, and J. A. Stroscio. Scattering and interference in epitaxial graphene. *Science*, 317(5835):219–222, 2007.
- [12] M. Sprinkle, D. Siegel, Y. Hu, J. Hicks, A. Tejada, A. Taleb-Ibrahimi, P. Le Fevre, F. Bertran, S. Vizzini, H. Enriquez et al. First direct observation of a nearly ideal graphene band structure. *Phys. Rev. Lett.*, 103(22):226803, 2009.
- [13] X. Li, W. Cai, J. An, S. Kim, J. Nah, D. Yang, R. Piner, A. Velamakanni, I. Jung, E. Tutuc et al. Large-area synthesis of high-quality and uniform graphene films on copper foils. *Science*, 324(5932):1312–1314, 2009.
- [14] S. Nie, M. W. Joseph, N. C. Bartelt, O. D. Dubon, and K. F. McCarty. Origin of the mosaicity in graphene grown on cu (111). *Phys. Rev. B*, 84(15):155425, 2011.

- [15] A. Varykhalov and O. Rader. Graphene grown on  $co(0001)$  films and islands: Electronic structure and its precise magnetization dependence. *Phys. Rev. B*, 80(3):035437, 2009.
- [16] T. Oznuluer, E. Pince, E. O. Polat, O. Balci, O. Salihoglu, and C. Kocabas. Synthesis of graphene on gold. *Appl. Phys. Lett.*, 98(18):183101, 2011.
- [17] J. W. McClure. Diamagnetism of graphite. *Phys. Rev.*, 104:666, 1956.
- [18] J. C. Slonczewski and P. R. Weiss. Band structure of graphite. *Phys. Rev.*, 109:272, 1958.
- [19] R. E. Smalley. Discovering the fullerenes. *Rev. Mod. Phys.*, 69(3):723–730, 1997.
- [20] S. Iijima et al. Helical microtubules of graphitic carbon. *nature*, 354(6348):56–58, 1991.
- [21] L. Brey and H. A. Fertig. Electronic states of graphene nanoribbons studied with the dirac equation. *Phys. Rev. B*, 73:235411, 2006.
- [22] W. Häusler and R. Egger. Artificial atoms in interacting graphene quantum dots. *Phys. Rev. B*, 80(16):161402, 2009.
- [23] Z. Z. Zhang, K. Chang, and F. M. Peeters. Tuning of energy levels and optical properties of graphene quantum dots. *Phys. Rev. B*, 77:235411, 2008.
- [24] K. Wakabayashi, Y. Takane, M. Yamamoto, and M. Sigrist. Electronic transport properties of graphene nanoribbons. *New J. Phys.*, 11(9):095016, 2009.
- [25] Motohiko Ezawa. Peculiar width dependence of the electronic properties of carbon nanoribbons. *Phys. Rev. B*, 73:045432, 2006.
- [26] Adam Rycerz, Electron transport and quantum-dot energy levels in Z-shaped graphene nanoconstriction with zigzag edges, *Acta Phys. Polon. A* 118, 238–243 (2010).
- [27] F. D. M. Haldane. Model for a quantum hall effect without landau levels: Condensed-matter realization of the “parity anomaly”. *Phys. Rev. Lett.*, 61:2015–2018, 1988.
- [28] Y. Zhang et al. Experimental observation of the quantum hall effect and berry’s phase in graphene. *Nature*, 438:201, 2005.
- [29] V. P. Gusynin and S. G. Sharapov. Unconventional integer quantum hall effect in graphene. *Phys. Rev. Lett.*, 95:146801, 2005.
- [30] Zhenhua Qiao, Shengyuan A. Yang, Wanxiang Feng, Wang-Kong Tse, Jun Ding, Yugui Yao, JianWang, and Qian Niu. Quantum anomalous hall effect in graphene from rashba and exchange effects. *Phys. Rev. B*, 82:161414, 2010.
- [31] Z. Qiao et al. Microscopic theory of quantum anomalous hall effect in graphene. *Phys. Rev. B*, 85:115439, 2012.
- [32] G. S. Diniz, M. R. Guassi, and F. Qu. Engineering the quantum anomalous hall effect in graphene with uniaxial strains. *J. Appl. Phys.*, 114(24), 2013.

- [33] C. L. Kane and E. J. Mele. Quantum spin hall effect in graphene. *Phys. Rev. Lett.*, 95(22):226801, 2005.
- [34] Yunyou Yang, Zhong Xu, L. Sheng, Baigeng Wang, D. Y. Xing, and D. N. Sheng. Time-reversal-symmetry-broken quantum spin hall effect. *Phys. Rev. Lett.*, 107:066602, 2011.
- [35] C. Chang, J. Zhang, X. Feng et al. Experimental observation of the quantum anomalous hall effect in a magnetic topological insulator. *Science*, 340:167, 2013.
- [36] X. Qi and S. Zhang. Topological insulators and superconductors. *Rev. Mod. Phys.*, 83:1057–1110, 2011.
- [37] R. Yu, W. Zhang, H. Zhang, S. Zhang, X. Dai, and Z. Fang. Quantized anomalous hall effect in magnetic topological insulators. *Science*, 329:61–4, 2010.
- [38] B. A. Bernevig, T. L. Hughes, and S. C. Zhang. Quantum spin hall effect and topological phase transition in hgte quantum wells. *Science*, 314(5806):1757–1761, 2006.
- [39] M. König, S. Wiedmann, C. Brüne, A. Roth, H. Buhmann, L. W. Molenkamp, Xiao-Liang. Qi, and Shou-Cheng Zhang. Quantum spin hall insulator state in hgte quantum wells. *Science*, 318(5851):766–770, 2007.
- [40] C. Liu, W. Feng, and Y. Yao. Quantum spin hall effect in silicene and two-dimensional germanium. *Phys. Rev. Lett.*, 107:076802, 2011.
- [41] X. Qian, J. Liu, L. Fu, and J. Li. Quantum spin hall effect in two-dimensional transition metal dichalcogenides. *Science*, 346:1344, 2014.
- [42] Ferry, D. K., Goodnick, S. M., Bird, J. (2009). *Transport in Nanostructures*. Cambridge University Press. DOI: 10.1017/CBO9780511840463.
- [43] C. L. Kane and E. J. Mele.  $z_2$  topological order and the quantum spin hall effect. *Phys. Rev. Lett.*, 95(14):146802, 2005.
- [44] C. Liu, T. L. Hughes, X. Qi, K. Wang, and S. Zhang. Quantum spin hall effect in inverted type-ii semiconductors. *Phys. Rev. Lett.*, 100:236601, 2008.
- [45] T. Chen, Z. Xiao, D. Chiou, and G. Guo. High chern number quantum anomalous hall phases in single-layer grapheme with Haldane orbital coupling. *Phys. Rev. B*, 84(16):165453, 2011.
- [46] S. Oh. The complete quantum hall trio. *Science*, 340(6129):153–154, 2013.
- [47] F. Guinea, M. I. Katsnelson, and A. K. Geim. Energy gaps and a zero-field quantum hall effect in graphene by strain engineering. *Nat. Phys.*, 6(1):30–33, 2009.
- [48] M. C. Rechtsman, J. M. Zeuner, A. Tünnermann, S. Nolte, M. Segev, and A. Szameit. Strain-induced pseudomagnetic field and photonic landau levels in dielectric structures. *Nature Photon.*, 3:91, 2009.

- [49] M. R. Guassi, G. S. Diniz, N. Sandler, and F. Qu. Zero-field and time-reversal-symmetry-broken topological phase transitions in graphene. *Phys. Rev. B*, 92:075426, 2015.
- [50] N. W. Ashcroft and N. D. Mermin. *Solid State Physics*. New York: Holt, Rinehart and Winston 1976.
- [51] A. H. Castro Neto, F. Guinea, N. M. R. Peres, K. S. Novoselov, and A. K. Geim. The electronic properties of graphene. *Rev. Mod. Phys.*, 81:109–162, 2009.
- [52] V. M. Pereira, A. H. Castro Neto, and N. M. R. Peres. Tight-binding approach to uniaxial strain in graphene. *Phys. Rev. B*, 80(4):045401, 2009.
- [53] Zhenhua Qiao, Wei Ren, Hua Chen, L. Bellaiche, Zhenyu Zhang, A. H. MacDonald, and Qian Niu. Quantum anomalous hall effect in graphene proximity coupled to an antiferromagnetic insulator. *Phys. Rev. Lett.*, 112:116404, 2014.
- [54] Adrian G. Swartz, Patrick M. Odenthal, Yufeng Hao, Rodney S. Ruoff, and Roland K. Kawakami. Integration of the ferromagnetic insulator EuO onto graphene. *ACS Nano*, 6(11):10063–10069, 2012.
- [55] Yugui Yao, Fei Ye, Xiao-Liang Qi, Shou-Cheng Zhang, and Zhong Fang. Spin-orbit gap of graphene: First-principles calculations. *Phys. Rev. B*, 75(4):041401, 2007.
- [56] J. C. Boettger and S. B. Trickey. First-principles calculation of the spin-orbit splitting in graphene. *Phys. Rev. B*, 75:121402, 2007.
- [57] H. Min, J. E. Hill, N. A. Sinitsyn, B. R. Sahu, L. Kleinman, and A. H. MacDonald. Intrinsic and Rashba spin-orbit interactions in graphene sheets. *Phys. Rev. B*, 74(16):165310, 2006.
- [58] N. M. R. Peres, F. Guinea, and A. H. Castro Neto. Coulomb interactions and ferromagnetism in pure and doped graphene. *Phys. Rev. B*, 72(17):174406, 2005.
- [59] A. H. Castro Neto and F. Guinea. Impurity-induced spin-orbit coupling in graphene. *Phys. Rev. Lett.*, 103:026804, 2009.
- [60] M. Zarea and N. Sandler. Rashba spin-orbit interaction in graphene and zigzag nanoribbons. *Phys. Rev. B*, 79(16):165442, 2009.
- [61] Daniel Huertas-Hernando, F. Guinea, and Arne Brataas. Spin-orbit coupling in curved graphene, fullerenes, nanotubes, and nanotube caps. *Phys. Rev. B*, 74:155426, 2006.
- [62] M. P. López-Sancho and M. C. Muñoz. Intrinsic spin-orbit interactions in flat and curved graphene nanoribbons. *Phys. Rev. B*, 83:075406, 2011.
- [63] Yu. S. Dedkov, M. Fonin, U. Rüdiger, and C. Laubschat. Rashba effect in the graphene/n(111) system. *Phys. Rev. Lett.*, 100:107602, 2008.
- [64] A. P. M. Barboza, A. P. Gomes, B. S. Archanjo, P. T. Araujo, A. Jorio, A. S. Ferlauto, M. S. C. Mazzoni, H. Chacham, and B. R. A. Neves. Deformation induced semiconductor-metal transition in single wall carbon nanotubes probed by electric force microscopy. *Phys. Rev. Lett.*, 100:256804, 2008.

- [65] Mingyuan Huang, Yang Wu, Bhupesh Chandra, Hugen Yan, Yuyao Shan, Tony F. Heinz, and James Hone. Direct measurement of strain-induced changes in the band structure of carbon nanotubes. *Phys. Rev. Lett.*, 100:136803, 2008.
- [66] A. G. Souza Filho, N. Kobayashi, J. Jiang, A. Grüneis, R. Saito, S. B. Cronin, J. Mendes Filho, Ge. G. Samsonidze, G. Dresselhaus, and M. S. Dresselhaus. Strain-induced interference effects on the resonance raman cross section of carbon nanotubes. *Phys. Rev. Lett.*, 95:217403, 2005.
- [67] Liu Yang and Jie Han. Electronic structure of deformed carbon nanotubes. *Phys. Rev. Lett.*, 85:154–157, 2000.
- [68] Jien Cao, Qian Wang, and Hongjie Dai. Electromechanical properties of metallic, quasimetallic, and semiconducting carbon nanotubes under stretching. *Phys. Rev. Lett.*, 90:157601, 2003.
- [69] Fang Liu, Pingbing Ming, and Ju Li. *Ab initio* calculation of ideal strength and phonon instability of graphene under tension. *Phys. Rev. B*, 76:064120, 2007.
- [70] K. S. Kim, Y. Zhao, H. Jang, S. Y. Lee, J. M. Kim, K. S. Kim, J. H. Ahn, P. Kim, J. Choi, and B. H. Hong. Large-scale pattern growth of graphene films for stretchable transparent electrodes. *Nature (London)*, 457:706, 2009.
- [71] L. Blakslee, D. G. Proctor, E. J. Seldin, G. B. Stence, and T. Wen. Elastic constants of compression-annealed pyrolytic graphite. *J. Appl. Phys*, 41:3373, 1970.
- [72] F. M. D. Pellegrino, G. G. N. Angilella, and R. Pucci. Strain effect on the optical conductivity of graphene. *Phys. Rev. B*, 81:035411, 2010.
- [73] H. Zhao, K. Min, and N. R. Aluru. Size and chirality dependent elastic properties of graphene nanoribbons under uniaxial tension. *Nano Letters*, 9(8):3012–3015, 2009.
- [74] Bitan Roy and Igor F. Herbut. Topological insulators in strained graphene at weak interaction. *Phys. Rev. B*, 88:045425, 2013.
- [75] Igor F. Herbut. Pseudomagnetic catalysis of the time-reversal symmetry breaking in graphene. *Phys. Rev. B*, 78:205433, 2008.
- [76] D. A. Abanin and D. A. Pesin. Interaction-induced topological insulator states in strained graphene. *Phys. Rev. Lett.*, 109:066802, 2012.
- [77] D. J. Thouless, M. Kohmoto, M. P. Nightingale, and M. den Nijs. Quantized hall conductance in a two-dimensional periodic potential. *Phys. Rev. Lett.*, 49:405–408, 1982.
- [78] Jeil Jung, Zhenhua Qiao, Qian Niu, and Allan H. MacDonald. Transport properties of graphene nanoroads in boron nitride sheets. *Nano Letters*, 12(6):2936–2940, 2012.
- [79] Vitor M. Pereira, A. H. Castro Neto, and N. M. R. Peres. Tight-binding approach to uniaxial strain in graphene. *Phys. Rev. B*, 80:045401, 2009.

- [80] Yasumasa Hasegawa, Rikio Konno, Hiroki Nakano, and Mahito Kohmoto. Zero modes of tight-binding electrons on the honeycomb lattice. *Phys. Rev. B*, 74:033413, 2006.
- [81] D. Bercioux and A. De Martino. Spin-resolved scattering through spin-orbit nanostructures in graphene. *Phys. Rev. B*, 81:165410, 2010.
- [82] Kyoko Nakada, Mitsutaka Fujita, Gene Dresselhaus, and Mildred S. Dresselhaus. Edge state in graphene ribbons: Nanometer size effect and edge shape dependence. *Phys. Rev. B*, 54:17954, 1996.
- [83] M. Oliva-Leyva and G. G. Naumis. Understanding electron behavior in strained graphene as a reciprocal space distortion. *Phys. Rev. B*, 88:085430, 2013.
- [84] Y. Lu and J. Guo. Band gap of strained graphene nanoribbons. *Nano Research*, 3(3):189–199, 2010.
- [85] D. A. Bahamon and Vitor M. Pereira. Conductance across strain junctions in graphene nanoribbons. *Phys. Rev. B*, 88:195416, 2013.
- [86] Ginetom S. Diniz, Marcos R. Guassi, and Fanyao Qu. Controllable spin-charge transport in strained graphene nanoribbon devices. *Journal of Applied Physics*, 116(11), 113705: 1–7, 2014.
- [87] Markus Morgenstern. Scanning tunneling microscopy and spectroscopy of graphene on insulating substrates. *physica status solidi (b)*, 248(11):2423–2434, 2011.
- [88] Elena Stolyarova, Kwang Taeg Rim, Sunmin Ryu, Janina Maultzsch, Philip Kim, Louis E. Brus, Tony F. Heinz, Mark S. Hybertsen, and George W. Flynn. High-resolution scanning tunneling microscopy imaging of mesoscopic graphene sheets on an insulating surface. *PNAS*, 104(22):9209–9212, 2007.
- [89] Guohong Li, Adina Luican-Mayer, Dmitry Abanin, Leonid Levitov, and Eva Y. Andrei. Evolution of landau levels into edge states in graphene. *Nat. Commun.*, 4:1744, 2013.
- [90] M. B. Nardelli. Electronic transport in extended systems: Application to carbon nanotubes. *Phys. Rev. B*, 60(11):7828, 1999.
- [91] M. P. Lopez Sancho, J. M. Lopez Sancho, and J. Rubio. Quick iterative scheme for the calculation of transfer matrices: application to mo (100). *Journal of Physics F: Metal Physics*, 14(5):1205, 1984.
- [92] R. Gómez-Medina, P. San José, A. García-Martín, M. Lester, M. Nieto-Vesperinas, and J. J. Sáenz. Resonant radiation pressure on neutral particles in a waveguide. *Phys. Rev. Lett.*, 86:4275–4277, 2001.
- [93] S. Datta and B. Das. Electronic analog of the electro-optic modulator. *Appl. Phys. Lett.*, 56(7):665–667, 1990.
- [94] J. Wurm, M. Wimmer, and K. Richter. Symmetries and the conductance of graphene nanoribbons with long-range disorder. *Phys. Rev. B*, 85:245418, 2012.